JM PAPERS

Formation of dry granular fronts and watery tails in debris flows

Xiannan Meng[1,2]**, C.G. Johnson**[2] **and J.M.N.T. Gray**[2],†

[1]Transportation Engineering College, Dalian Maritime University, Dalian 116026, PR China

[2]Department of Mathematics and Manchester Centre for Nonlinear Dynamics, University of Manchester, Oxford Road, Manchester M13 9PL, UK

Debris flows are particle–fluid mixtures that pose a significant hazard to many communities throughout the world. Bouldery debris flows are often characterised by a deep dry granular flow front, which is followed by a progressively thinner and increasingly watery tail. The formation of highly destructive bouldery wave fronts is usually attributed to particle-size segregation. However, the moving-bed flume experiments of Davies (*N. Z. J. Hydrol.*, vol. 29, 1990, pp. 18–46) show that discrete surges with dry fronts and watery tails also form in monodisperse particle–fluid mixtures. These observations motivate the development of a new depth-averaged mixture theory for debris flows, which explicitly takes account of the differing granular and phreatic surfaces, velocity shear, and relative motion between grains and fluid to explain these phenomena. The theory consists of four coupled conservation laws that describe the spatial and temporal evolution of the grain and water thicknesses and depth-averaged velocities. This system enables travelling wave solutions to be constructed that consist of (i) a large amplitude dry flow front that smoothly transitions to (ii) an undersaturated body, (iii) an oversaturated region and then (iv) a pure water tail. It is shown that these solutions are in good quantitative agreement with Davies' experiments at high bed speeds and slope inclinations. At lower bed speeds and inclinations, the theory produces travelling wave solutions that connect to a steady-uniform upstream flow, and may or may not have a bulbous flow front, consistent with Davies' observations.

Key words: wet granular material, geophysical and geological flows

1. Introduction

Debris flows have attracted the attention of scientists due to the catastrophic nature of the hazards that they pose (Iverson 1997; McSaveney, Beetham & Leonard 2005).

† Email address for correspondence: nico.gray@manchester.ac.uk

A devastating example is that of the 8 August 2010 debris flow in the northwestern Chinese province of Gansu, which caused more than 1000 deaths in the county of Zhouqu (Ren 2014). Two other prominent recent examples are when heavy rainfall triggered 107 debris flows in Hiroshima city in southwest Japan on 20 August 2014 (Wang *et al.* 2015), which caused 44 injuries and 74 deaths, as well as a torrent of rock, ice, sediment and water in Uttarakhand in northern India (Sati 2022), which killed hundreds of people and devastated two hydropower stations on 7 February 2021. In recent years, debris flow frequency has increased, due to the increased intensity of rainfall events (Ballantyne 2002), glacial melt water, severe forest fires (Kean *et al.* 2019) and the melting of permafrost (Higman *et al.* 2018), which has made previously stable slopes unstable. This provides strong motivation for the study of the dynamics of debris flows, with the goal of minimising damage to people and infrastructure.

One of the most destructive features of debris flows is the initial deep surge, which is drier than the main body and is often rich in boulders and larger particles. A typical example is shown in figure 1(*a*) and the supplementary online video (movie 1) available at https://doi.org/10.1017/jfm.2022.400, where a very rapidly moving debris front narrowly misses a group of hikers in Aconcagua Park in Argentina. After the initial bouldery surge, the flow slowly wanes in height at the same time as the largest surface grains decrease in size and the flow becomes increasingly watery (figure 1*b*). A series of secondary drier boulder-rich surges that transition to watery tails then propagate down the channel at 40, 71 and 160 seconds. These poorly understood phenomena are often observed in the field (Costa & Williams 1984; Pierson 1986; Kean *et al.* 2013) and in large-scale debris-flow experiments (Iverson *et al.* 2010; Johnson *et al.* 2012). Closely related flow features can also develop in suspensions (Murisic *et al.* 2013), snow avalanches (Gray & Hutter 1997) and pyroclastic flows (Mangeney *et al.* 2007), as well as in small-scale wet and dry analogue experiments (Félix & Thomas 2004; Woodhouse *et al.* 2012; Kokelaar *et al.* 2014; de Haas *et al.* 2015; Scheidl, McArdell & Rickenmann 2015; Baker, Johnson & Gray 2016*a*; Lanzoni, Gregoretti & Stancanelli 2017).

Since the water typically experiences less friction than the grains, many existing debris flow models predict that water moves to the front of the flow (George & Iverson 2011; Pudasaini 2012). As a result, the formation of dry snouts is often attributed to particle-size segregation (see Vallance & Savage 2000; Gray & Ancey 2009; Iverson *et al.* 2010; Johnson *et al.* 2012; George & Iverson 2014; Baker *et al.* 2016*a*; Liu *et al.* 2020) and the two ideas have become conflated. Certainly, the vertical ordering provided by particle-size segregation (i.e. that during shear, large particles tend to rise above finer grains) combined with velocity shear leads to differential longitudinal transport of the large and small particles and the formation of a bouldery snout (Gray & Ancey 2009; Gray & Kokelaar 2010; Johnson *et al.* 2012; Gray 2018), but there is no clear reason why the snout should be dry.

The moving bed flume experiments of Davies (1988, 1990), with monodisperse-particle–fluid mixtures, show that dry fronts can develop even in the absence of particle segregation. Similar dry fronts also develop in monodisperse-particle–fluid mixtures in rotating drums (Leonardi *et al.* 2015) and on chutes (Taylor-Noonan 2020). This implies that the dry snouts do not require particle-size segregation, which motivates the development, in this paper, of a new depth-averaged model for monodisperse-particle–fluid mixtures that can account for their formation. As with particle-size segregation, vertical structure and velocity shear will play a key role in its derivation.

Despite its importance, velocity shear is completely neglected in most debris-flow models which assume plug flow through their depth (Iverson 1997; Iverson & Denlinger 2001; Pitman & Le 2005; Pailha & Pouliquen 2008; Pudasaini 2012; Iverson & George

(*a*)

(*b*)

Figure 1. Debris flow on 27 January 2015 in Aconcagua Park, Mendoza, Argentina (copyright Julian Insarralde via ViralHog). (*a*) A large amplitude dry bouldery flow front propagates down a channel at approximately 6 m s^{-1}, forcing hikers to scramble to safety. (*b*) Eighteen seconds later, the height of the flow has reduced, there are no surface boulders and the flow is much more watery. Movie 1 in the online supplementary material shows that the main pulse is followed by a series of bouldery surges, 40, 71 and 160 seconds after the arrival of the main front, which are interspersed by lower amplitude watery sections.

2014; Bouchut *et al.* 2016). Johnson *et al.*'s (2012) large-scale debris-flow experiments at the United States Geological Survey (USGS) flume show that there is in fact strong internal velocity shear through the flow depth. The flow spread out strongly along the main body of the chute, and entered a locally quasi-steady depositional regime as the front propagated down the run-out pad. In this part of the flow, typical measured surface velocities in the centre of the channel were of the order of $6\text{--}8 \text{ m s}^{-1}$, while the front propagated steadily downslope at 2 m s^{-1}. Material that reached the front was either overridden by the flow itself, or shouldered aside to form static lateral levees that channelised the oncoming flow. Detailed movies showing the flow structure and the process by which the levees were emplaced are available in the online supplementary material of Johnson *et al.* (2012). There are also a series of informative video clips showing strong velocity shear and particle recirculation at the front of debris flows in the open file report of Costa & Williams (1984).

Depth-averaged theories for dry granular avalanches are well established and exploit the shallowness of the flow to derive conservation laws for the avalanche depth h and the depth-averaged velocity $\bar{\boldsymbol{u}}$ (Savage & Hutter 1989; Gray, Wieland & Hutter 1999;

Pouliquen 1999*b*; Gray, Tai & Noelle 2003; Gray & Edwards 2014). However, the presence of the interstitial water significantly alters the flow behaviour and it is therefore included in two-phase depth-averaged models for debris flows (Iverson & Denlinger 2001; Pitman & Le 2005; Pailha & Pouliquen 2008; Pudasaini 2012; Kowalski & McElwaine 2013; Iverson & George 2014; Bouchut *et al.* 2016). The model of Pitman & Le (2005) couples the grains and the water through buoyancy and drag interaction forces, and the virtual mass interaction force is also added in the model of Pudasaini (2012). The buoyancy reduces the effective weight of the grains, thereby reducing the effective stress and the granular basal friction. The drag force occurs due to the relative motion of the flowing materials. In the depth-averaged model of Iverson & George (2014), the basal granular friction is reduced (or enhanced) as a positive (or negative) excess pore fluid pressure is generated due to changes in the solids volume fraction.

As mentioned earlier, most debris-flow models are built on the assumption of a plug-like velocity profile. However, when both the species' concentration and downslope velocity vary over the flow depth, the resulting depth-averaged velocities of grains and water may differ, even if the local velocity of grains and water are identical. When the depth-averaged velocity of the grains is faster than the depth-averaged velocity of the water, grains are transported to the flow front and may accumulate to form a dry snout. The two-phase flow model of Berzi *et al.* (2009, 2010) captures such shear-induced transport, using a granular-fluid rheology to determine the velocity profile of the mixture and assuming a simple vertical structure. In addition, Kowalski & McElwaine (2013) describe shear-induced transport, but focus on the evolving vertical structure of the flow due to sedimentation and resuspension processes.

Inspired by the experimental observations of Davies (1988, 1990) and Johnson *et al.* (2012), this paper derives a two-phase depth-averaged debris flow model that combines shear-induced transport, and a relative motion between the grains and fluid. The model describes separate free surfaces for water and grains, allowing for both oversaturated and undersaturated flows, where the water free surface lies above or below the free surface of the grains. The combination of this layered structure with velocity shear results in a shear-induced transport of grains or fluid forwards or backwards in the flow even when, locally, the two phases have identical velocity (Gray & Kokelaar 2010). Here, however, the local percolation of fluid through the grains is also modelled. The resulting difference between granular and fluid velocities, although often much smaller than the typical flow speed, provides a second mechanism for differential transport of the two phases, which may augment or oppose the shear-induced transport. It is the combination of these two mechanisms that allows the model to describe the steadily travelling finite granular mass solutions that Davies (1988, 1990) observed in his moving bed flume. These transition smoothly from a dry front to an undersaturated region, an oversaturated region and finally a pure watery tail, which is closely akin to what is observed in the field (Pierson 1986; Iverson 1997; Kean *et al.* 2013).

2. Governing equations

2.1. *Mixture framework*

Continuum mixture theory (Truesdell 1984; Morland 1992) provides a framework to describe the motion of multi-phase materials and postulates that each spatial point is simultaneously occupied by all the phases. Debris flows may be composed of grains, water and air, but for simplicity, this paper uses a two-phase formulation that neglects the effect of air. The volume fraction ϕ^ν of constituent ν determines what proportion of the mixture

volume is occupied by that constituent. Using the constituent letters $\nu = w, g$ for water and grains, respectively, it follows that for a pure water phase, $\phi^w = 1$, while for a dry granular phase, the solids volume fraction $\phi^g < 1$ and $\phi^w = 0$. However, for a water saturated flow, the volume fractions sum to unity

$$\phi^g + \phi^w = 1. \tag{2.1}$$

Mixture theory defines overlapping partial density ϱ^ν, partial velocity $\boldsymbol{u}^\nu$ and partial stress $\boldsymbol{\sigma}^\nu$ fields for each phase. Each distributed phase satisfies its individual conservation laws for mass,

$$\frac{\partial \varrho^\nu}{\partial t} + \boldsymbol{\nabla} \cdot (\varrho^\nu \boldsymbol{u}^\nu) = 0, \tag{2.2}$$

and for momentum,

$$\frac{\partial}{\partial t}(\varrho^\nu \boldsymbol{u}^\nu) + \boldsymbol{\nabla} \cdot (\varrho^\nu \boldsymbol{u}^\nu \otimes \boldsymbol{u}^\nu) = \boldsymbol{\nabla} \cdot \boldsymbol{\sigma}^\nu + \varrho^\nu \boldsymbol{g} + \boldsymbol{\beta}^\nu, \tag{2.3}$$

where t is time, $\boldsymbol{\nabla}$ is the gradient operator, $\cdot$ is the dot product, $\otimes$ is the dyadic product and $\boldsymbol{g}$ the acceleration due to gravity. The interaction drag $\boldsymbol{\beta}^\nu$ is the force exerted on the ν phase by the other phase, and satisfies $\boldsymbol{\beta}^g + \boldsymbol{\beta}^w = 0$ according to Newton's third law.

The partial density is related to its intrinsic counterpart (defined on a unit volume of that constituent) by a linear volume fraction scaling, while the partial and intrinsic velocity fields are identical

$$\varrho^\nu = \phi^\nu \varrho^{\nu\star}, \quad \boldsymbol{u}^\nu = \boldsymbol{u}^{\nu\star}, \tag{2.4a,b}$$

where the superscript $\star$ represents an intrinsic quantity. The intrinsic pore fluid pressure in the water is $p^{w\star}$. Following de Boer & Ehlers (1990), the partial stress in the grains is decomposed into

$$\boldsymbol{\sigma}^g = -\phi^g p^{w\star} \mathbf{1} - \boldsymbol{\sigma}^e, \tag{2.5}$$

where $\boldsymbol{\sigma}^e$ is the effective stress (which, by the convention used in soil mechanics, has the opposite sign to that of Cauchy stress) and $\mathbf{1}$ is the unit tensor. The partial water stress is assumed to be

$$\boldsymbol{\sigma}^w = -\phi^w p^{w\star} \mathbf{1} + \boldsymbol{\tau}^w, \tag{2.6}$$

where the deviatoric stress $\boldsymbol{\tau}^w$ satisfies a Newtonian fluid law

$$\boldsymbol{\tau}^w = \phi^w \eta^w (\boldsymbol{\nabla} \boldsymbol{u}^w + (\boldsymbol{\nabla} \boldsymbol{u}^w)^{\mathrm{T}}), \tag{2.7}$$

in which η^w is the dynamic viscosity and T is the transpose. This assumes that the interstitial fluid can be described as a Newtonian fluid with constant viscosity, which is a potential source of discrepancy. For instance, in Baumgarten & Kamrin's (2019) two-phase fluid–sediment mixture model, Einstein's (1906) linear solids volume correction is used to account for the increased viscosity of the fluid due to the suspended sediment. This idea can be extended to higher solids volume fractions. For instance, Boyer, Guazzelli & Pouliquen (2011) showed how to relate the frictional behaviour of dense suspensions with classical viscous suspension rheology, so that their behaviour could be expressed either as a function of the solids volume fraction or the viscous number $I_v = J = \eta^w \dot{\gamma} / p^g$, where $\dot{\gamma}$ is the shear rate and p^g is the pressure due to grain contacts. This suspension rheology works well at low shear rates, but at higher shear rates, it has been found that there is a transition towards a dependence on the granular inertial number $I = \dot{\gamma} d / \sqrt{p^g / \varrho^{g\star}}$ (Trulsson, Andreotti & Claudin 2012; Maurin, Chauchat & Frey 2016). While these

suspension rheologies determine the composite response for a single effective medium, it is by no means clear how to partition the stress back between the individual phases.

Equations (2.6) and (2.7) are consistent with the mixture theory approach of Nunziato *et al.* (1986), although an ensemble averaging approach is also possible (Anderson & Jackson 1967; Joseph & Lungdren 1990; Anderson, Sundaresan & Jackson 1995; Enwald, Pelrano & Almstedt 1996; Jackson 2000). The sum of the partial solid and fluid stresses, (2.5) and (2.6), determines the total stress

$$\boldsymbol{\sigma}^{total} = -p^{w\star}\mathbf{1} - \boldsymbol{\sigma}^e + \boldsymbol{\tau}^w, \tag{2.8}$$

which is consistent with the effective stress principle of soil mechanics (Terzaghi 1943). It also agrees with the experimental observation that the manometric pressure in the soil is the pressure as if the medium were a bulk fluid, unaffected by the presence of the solid constituent in the medium.

The interaction drags acting on the water and grain phases are defined by

$$\boldsymbol{\beta}^w = -\boldsymbol{\beta}^g = p^{w\star}\boldsymbol{\nabla}\phi^w + C^d(\boldsymbol{u}^g - \boldsymbol{u}^w), \tag{2.9}$$

where the term $p^{w\star}\boldsymbol{\nabla}\phi^w$ combines with the partial water pressure gradient $-\boldsymbol{\nabla}(\phi^w p^{w\star})$ in the water momentum balance (2.3) to ensure that the fluid is driven by gradients in the intrinsic pore water pressure $-\phi^w\boldsymbol{\nabla}p^{w\star}$, consistent with Darcy's law (Bear 1972; Morland 1992). The second term on the right-hand side of (2.9) is the drag due to the relative motion of the grains and water, with drag coefficient

$$C^d = \eta^w\frac{(\phi^w)^2}{k}, \quad \text{where the permeability } k = \frac{(\phi^w)^3 d^2}{180(\phi^g)^2}, \tag{2.10}$$

is given by Carman's formula for the packing of spheres of diameter d. This agrees well with the sediment dynamics experiments of Goharzadeh, Khalili & Jørgensen (2005) and Ouriemi, Aussillous & Guazzelli (2009).

When the constitutive laws (2.5) and (2.6) and the interaction drags (2.9) are substituted into (2.3), the momentum balance equations for the grains and the fluid take the form

$$\frac{\partial}{\partial t}(\varrho^g\boldsymbol{u}^g) + \boldsymbol{\nabla}\cdot(\varrho^g\boldsymbol{u}^g\otimes\boldsymbol{u}^g) = -\boldsymbol{\nabla}\cdot\boldsymbol{\sigma}^e - \phi^g\boldsymbol{\nabla}p^{w\star} + \varrho^g\boldsymbol{g} + C^d(\boldsymbol{u}^w - \boldsymbol{u}^g), \tag{2.11}$$

$$\frac{\partial}{\partial t}(\varrho^w\boldsymbol{u}^w) + \boldsymbol{\nabla}\cdot(\varrho^w\boldsymbol{u}^w\otimes\boldsymbol{u}^w) = -\phi^w\boldsymbol{\nabla}p^{w\star} + \boldsymbol{\nabla}\cdot\boldsymbol{\tau}^w + \varrho^w\boldsymbol{g} + C^d(\boldsymbol{u}^g - \boldsymbol{u}^w), \tag{2.12}$$

assuming that the mixture is fully saturated. When there is no water ($\phi^w = 0$), the buoyancy force $-\phi^g\boldsymbol{\nabla}p^{w\star}$ and the Darcy interaction force $C^d(\boldsymbol{u}^w - \boldsymbol{u}^g)$ are assumed to be zero, and the momentum balance (2.11) then reduces to that for dry grains. Conversely, in the case of pure water ($\phi^w = 1$), (2.12) naturally reduces to the Navier–Stokes equations. The momentum balances (2.11) and (2.12) are identical to those employed to investigate debris flows by Iverson & Denlinger (2001), sediment flows by Ouriemi *et al.* (2009) and general fluid–sediment flows by Baumgarten & Kamrin (2019), apart from the particular choices of the Darcy drag coefficients and effective fluid phase viscosity.

2.2. *Boundary conditions*

A Cartesian coordinate system *Oxz* is introduced with the *x*-axis pointing down a slope inclined at an angle ζ to the horizontal and with the *z*-axis pointing upwards, as shown in figure 2. A third coordinate *y*, lying across the slope, can easily be added to model fully
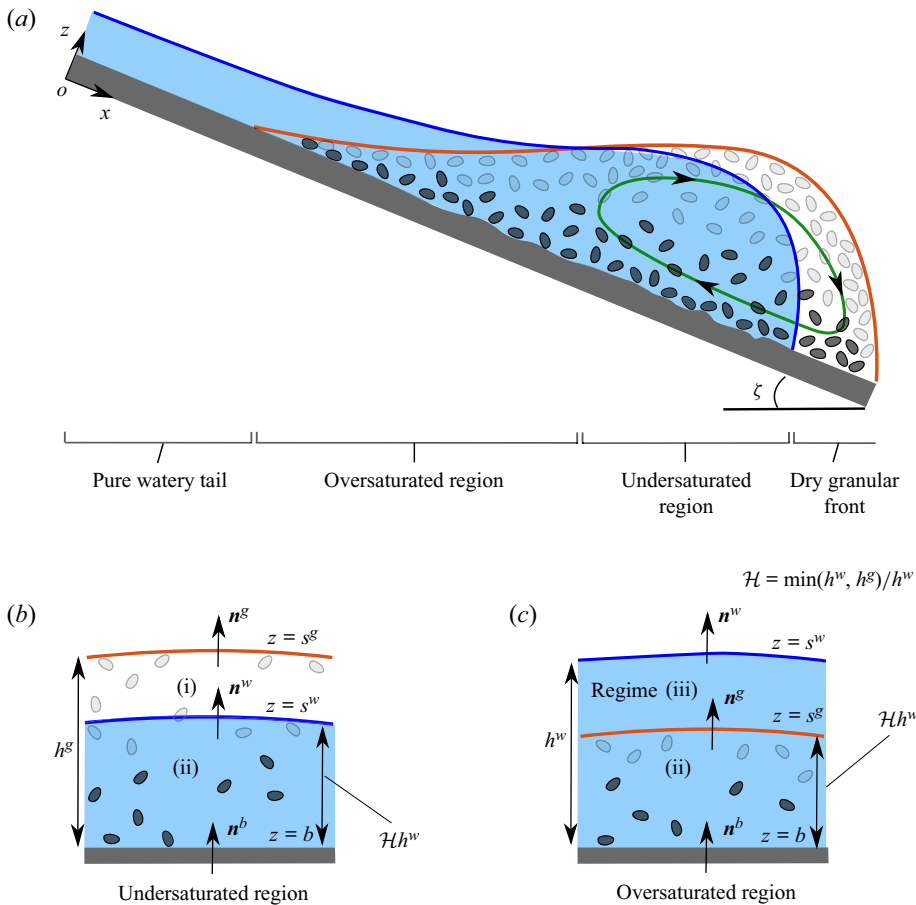
Figure 2. (*a*) Two-dimensional schematic diagram of a debris flow on a slope inclined at an angle ζ to the horizontal. Blue shading corresponds to water, while the grains occupy the region below the red free surface. Velocity shear results in the surface layer of (light) grains moving towards the front, while the (dark) grains near the base move backwards relative to the front. This creates a recirculating (green) frontal cell. The water free surface (blue) and the granular free surface (red) do not coincide. The debris flow therefore consists of a dry granular front, an undersaturated wet flow, an oversaturated wet flow and a pure watery tail. It is useful to resolve the vertical structure as shown in panels (*b,c*) for the undersaturated and oversaturated regimes. In panel (*b*), the granular free surface at $z = s^g(x, t)$ is above the water free surface at $z = s^w(x, t)$, while in the oversaturated regime, the situation is reversed. The base of the flow lies at $z = b(x)$ and the water and grain heights are $h^w = s^w - b$ and $h^g = s^g - b$. The internal interface height is $\min(h^g, h^w)$ and the proportion of the water flow height that is occupied by grains is equal to $\mathcal{H} = \min(h^g, h^w)/h^w$. Within this vertical structure, region (i) consists of dry grains, region (ii) is a mixture of grains and water, and region (iii) is pure water.

three-dimensional flows, but for ease of exposition, the theory presented here is purely two-dimensional. The debris flow is assumed to have velocity components $\boldsymbol{u}^\nu = (u^\nu, w^\nu)$ in the downslope and slope normal directions, respectively. The grain surface is defined by the function $F^g(z, x, t) = z - s^g(x, t)$, the water surface by $F^w(z, x, t) = z - s^w(x, t)$ and the basal surface by $F^b(z, x, t) = z - b(x)$. It follows that the upward pointing unit normal for each surface is $\boldsymbol{n}^\nu = \nabla F^\nu/|\nabla F^\nu|$, where $\nu = g, w, b$. In the undersaturated regime (figure 2*b*), the water surface is below the grain surface, i.e. $s^w < s^g$, whereas in the oversaturated regime (figure 2*c*), the water surface is above it, i.e. $s^g < s^w$.

The grain phase is subject to kinematic conditions on the grain surface $F^g(x, t) = 0$ and the basal surface $F^b(x) = 0$. These conditions are given by

$$\frac{\partial F^g}{\partial t} + \boldsymbol{u}^g \cdot \nabla F^g = 0, \quad F^g(x, t) = 0, \tag{2.13}$$

$$\frac{\partial F^b}{\partial t} + \boldsymbol{u}^g \cdot \nabla F^b = 0, \quad F^b(x) = 0. \tag{2.14}$$

Similarly, the water phase is subject to kinematic conditions on the water surface $F^w(x, t) = 0$ and the basal surface $F^b(x) = 0$. They are given by

$$\frac{\partial F^w}{\partial t} + \boldsymbol{u}^w \cdot \nabla F^w = 0, \quad F^w(x, t) = 0, \tag{2.15}$$

$$\frac{\partial F^b}{\partial t} + \boldsymbol{u}^w \cdot \nabla F^b = 0, \quad F^b(x) = 0. \tag{2.16}$$

Grains can penetrate the water surface in the undersaturated regime (figure 2*b*) and water can penetrate the grain surface in the oversaturated regime (figure 2*c*). The material that crosses these surfaces can change its volume fraction abruptly, e.g. in the oversaturated regime, the volume fraction of water jumps from $\phi^w = 1 - \phi^g$ to $\phi^w = 1$ across the interface. To describe such singular interfaces, the mass jump conditions (Chadwick 1976) are

$$[\![\varrho^g(\boldsymbol{u}^g - \boldsymbol{u}^w) \cdot \boldsymbol{n}^w]\!] = 0, \quad F^w(x, t) = 0, \tag{2.17}$$

$$[\![\varrho^w(\boldsymbol{u}^w - \boldsymbol{u}^g) \cdot \boldsymbol{n}^g]\!] = 0, \quad F^g(x, t) = 0, \tag{2.18}$$

where the jump brackets $[\![\ ]\!]$ indicate the difference between the enclosed quantity on the forward $(+)$ and rearward $(-)$ sides of the discontinuity. Equation (2.17) describes the conservation of grains across the water free surface in the undersaturated case, while (2.18) describes the conservation of water across the granular free surface in the oversaturated regime.

Grains and water satisfy traction-free conditions at their free surfaces

$$\boldsymbol{\sigma}^e \boldsymbol{n}^g = \boldsymbol{0}, \quad F^g(x, t) = 0, \tag{2.19}$$

$$\boldsymbol{\sigma}^w \boldsymbol{n}^w = \boldsymbol{0}, \quad F^w(x, t) = 0. \tag{2.20}$$

Iverson (2003) used large-scale debris flow flume tests to show that the grain phase experiences a Coulomb-type friction. Additionally, the Chézy formula (Chaudhry 2008), an empirically derived expression to take into account turbulent friction arising from the bottom of the channel, can be employed to describe the basal friction experienced by the water phase. The solid bed friction and Chézy formula take the form

$$\boldsymbol{\sigma}^e \boldsymbol{n}^b - (\boldsymbol{n}^b \cdot \boldsymbol{\sigma}^e \boldsymbol{n}^b)\boldsymbol{n}^b = -\frac{\boldsymbol{u}_b^g}{|\boldsymbol{u}_b^g|}\mu^b(\boldsymbol{n}^b \cdot \boldsymbol{\sigma}^e \boldsymbol{n}^b), \quad F^b(x) = 0, \tag{2.21}$$

$$\boldsymbol{\sigma}^w \boldsymbol{n}^b - (\boldsymbol{n}^b \cdot \boldsymbol{\sigma}^w \boldsymbol{n}^b)\boldsymbol{n}^b = \varrho^{w\star} C^w |\bar{\boldsymbol{u}}^w| \bar{\boldsymbol{u}}^w, \quad F^b(x) = 0, \tag{2.22}$$

where μ^b is the basal friction coefficient, C^w is the Chézy drag coefficient (Hogg & Pritchard 2004) and $\bar{\boldsymbol{u}}^w$ is the depth-averaged water velocity. Detailed formulae for the coefficients μ^b and C^w will be discussed after the depth-integration process.

943 A19-8

3. Non-dimensionalisation

3.1. *Scaling the governing equations*

Debris flows typically have a flow depth H that is much smaller than their length L. This makes it possible to derive a depth-averaged model, which does not depend on the normal coordinate z. Typical downstream flow speeds for both the grain and water phases are assumed to be of the order of the gravity wave speed $U = (gH)^{1/2}$, and the mass balances then imply that typical normal velocities are of magnitude εU, where the aspect ratio $\varepsilon = H/L \ll 1$. Hydrostatic and lithostatic balances for the pore fluid pressure and the grain normal stresses suggest scalings of $\varrho^{w\star} gH$ and $\varrho^{g\star} gH$, respectively. A Coulomb friction law then suggests that the typical order of magnitude for the grain shear stress is $\mu \varrho^{g\star} gH$, where μ is the friction coefficient. The scaling of the deviatoric water stress is determined by the Newtonian constitutive law (2.7). The governing equations and boundary conditions are therefore non-dimensionalised by the scalings

$$
\left.
\begin{aligned}
(x, z, s^w, s^g, b, d) &= L(\hat{x}, \varepsilon\hat{z}, \varepsilon\hat{s}^w, \varepsilon\hat{s}^g, \varepsilon\hat{b}, \varepsilon\hat{d}), \quad t = L/(gH)^{1/2}\hat{t}, \\
(u^v, w^v, |\boldsymbol{u}^v|) &= (gH)^{1/2}(\hat{u}^v, \varepsilon\hat{w}^v, |\hat{\boldsymbol{u}}^v|), \quad C^d = \varrho^{w\star}(g/H)^{1/2}\hat{C}^d, \\
(\sigma_{xx}^e, \sigma_{zz}^e, \sigma_{xz}^e) &= \varrho^{g\star} gH(\hat{\sigma}_{xx}^e, \hat{\sigma}_{zz}^e, \mu\hat{\sigma}_{xz}^e), \\
(p^{w\star}, \tau_{xx}^w, \tau_{zz}^w, \tau_{xz}^w) &= \varrho^{w\star} gH(\hat{p}^{w\star}, \varepsilon\hat{\tau}_{xx}^w, \varepsilon\tau_{zz}^w, \hat{\tau}_{xz}^w),
\end{aligned}
\right\} \quad (3.1a\text{–}f)
$$

where the hatted quantities are non-dimensional. These scalings imply that for the grains, the non-dimensional mass and momentum balance components are

$$
\frac{\partial \phi^g}{\partial \hat{t}} + \frac{\partial}{\partial \hat{x}}(\phi^g \hat{u}^g) + \frac{\partial}{\partial \hat{z}}(\phi^g \hat{w}^g) = 0, \tag{3.2}
$$

$$
\varepsilon\left(\frac{\partial}{\partial \hat{t}}(\phi^g \hat{u}^g) + \frac{\partial}{\partial \hat{x}}(\phi^g \hat{u}^g \hat{u}^g) + \frac{\partial}{\partial \hat{z}}(\phi^g \hat{u}^g \hat{w}^g)\right)
$$
$$
= -\varepsilon\gamma\phi^g\frac{\partial \hat{p}^{w\star}}{\partial \hat{x}} - \varepsilon\frac{\partial \hat{\sigma}_{xx}^e}{\partial \hat{x}} - \mu\frac{\partial \hat{\sigma}_{xz}^e}{\partial \hat{z}} + \phi^g \sin\zeta + \gamma\hat{C}^d(\hat{u}^w - \hat{u}^g), \tag{3.3}
$$

$$
\varepsilon^2\left(\frac{\partial}{\partial \hat{t}}(\phi^g \hat{w}^g) + \frac{\partial}{\partial \hat{x}}(\phi^g \hat{u}^g \hat{w}^g) + \frac{\partial}{\partial \hat{z}}(\phi^g \hat{w}^g \hat{w}^g)\right)
$$
$$
= -\gamma\phi^g\frac{\partial \hat{p}^{w\star}}{\partial \hat{z}} - \varepsilon\mu\frac{\partial \hat{\sigma}_{xz}^e}{\partial \hat{x}} - \frac{\partial \hat{\sigma}_{zz}^e}{\partial \hat{z}} - \phi^g \cos\zeta + \varepsilon\gamma\hat{C}^d(\hat{w}^w - \hat{w}^g), \tag{3.4}
$$

where the density ratio

$$
\gamma = \varrho^{w\star}/\varrho^{g\star}. \tag{3.5}
$$

Similarly, the non-dimensional water mass balance and the downslope and normal components of the momentum balance are given by

$$
\frac{\partial \phi^w}{\partial \hat{t}} + \frac{\partial}{\partial \hat{x}}(\phi^w \hat{u}^w) + \frac{\partial}{\partial \hat{z}}(\phi^w \hat{w}^w) = 0, \tag{3.6}
$$

$$
\varepsilon\left(\frac{\partial}{\partial \hat{t}}(\phi^w \hat{u}^w) + \frac{\partial}{\partial \hat{x}}(\phi^w \hat{u}^w \hat{u}^w) + \frac{\partial}{\partial \hat{z}}(\phi^w \hat{u}^w \hat{w}^w)\right)
$$

$$= -\varepsilon \phi^w \frac{\partial \hat{p}^{w\star}}{\partial \hat{x}} + \varepsilon^2 \frac{\partial \hat{\tau}_{xx}^w}{\partial \hat{x}} + \frac{\partial \hat{\tau}_{xz}^w}{\partial \hat{z}} + \phi^w \sin \zeta - \hat{C}^d (\hat{u}^w - \hat{u}^g), \tag{3.7}$$

$$\varepsilon^2 \left(\frac{\partial}{\partial \hat{t}} (\phi^w \hat{w}^w) + \frac{\partial}{\partial \hat{x}} (\phi^w \hat{u}^w \hat{w}^w) + \frac{\partial}{\partial \hat{z}} (\phi^w \hat{w}^w \hat{w}^w) \right)$$

$$= -\phi^w \frac{\partial \hat{p}^{w\star}}{\partial \hat{z}} + \varepsilon \frac{\partial \hat{\tau}_{xz}^w}{\partial \hat{x}} + \varepsilon \frac{\partial \hat{\tau}_{zz}^w}{\partial \hat{z}} - \phi^w \cos \zeta - \varepsilon \hat{C}^d (\hat{w}^w - \hat{w}^g). \tag{3.8}$$

3.2. *Non-dimensional boundary conditions*

The non-dimensional kinematic conditions (2.13) and (2.14) for the grains are

$$\frac{\partial \hat{s}^g}{\partial \hat{t}} + \hat{u}^g \frac{\partial \hat{s}^g}{\partial \hat{x}} - \hat{w}^g = 0, \quad \hat{z} = \hat{s}^g(\hat{x}, \hat{t}), \tag{3.9}$$

$$\frac{\partial \hat{b}}{\partial \hat{t}} + \hat{u}^g \frac{\partial \hat{b}}{\partial \hat{x}} - \hat{w}^g = 0, \quad \hat{z} = \hat{b}(\hat{x}), \tag{3.10}$$

and the non-dimensional kinematic conditions (2.15) and (2.16) for the water are

$$\frac{\partial \hat{s}^w}{\partial \hat{t}} + \hat{u}^w \frac{\partial \hat{s}^w}{\partial \hat{x}} - \hat{w}^w = 0, \quad \hat{z} = \hat{s}^w(\hat{x}, \hat{t}), \tag{3.11}$$

$$\frac{\partial \hat{b}}{\partial \hat{t}} + \hat{u}^w \frac{\partial \hat{b}}{\partial \hat{x}} - \hat{w}^w = 0, \quad \hat{z} = \hat{b}(\hat{x}). \tag{3.12}$$

To formulate the non-dimensional form of the mass-jump conditions (2.17) and (2.18), the kinematic conditions (2.15) and (2.13) are used to show that $\boldsymbol{u}^w \cdot \boldsymbol{n}^w = -(\partial F^w / \partial t) \cdot (1/|\nabla F^w|)$ and $\boldsymbol{u}^g \cdot \boldsymbol{n}^g = -(\partial F^g / \partial t) \cdot (1/|\nabla F^g|)$. Substitution of these results implies that the non-dimensional jump conditions at the undersaturated water free surface and the oversaturated grain free surface are

$$\left[\!\left[\phi^g \left(\frac{\partial \hat{s}^w}{\partial \hat{t}} + \hat{u}^g \frac{\partial \hat{s}^w}{\partial \hat{x}} - \hat{w}^g \right) \right]\!\right] = 0, \quad \hat{z} = \hat{s}^w(\hat{x}, \hat{t}), \tag{3.13}$$

$$\left[\!\left[\phi^w \left(\frac{\partial \hat{s}^g}{\partial \hat{t}} + \hat{u}^w \frac{\partial \hat{s}^g}{\partial \hat{x}} - \hat{w}^w \right) \right]\!\right] = 0, \quad \hat{z} = \hat{s}^g(\hat{x}, \hat{t}). \tag{3.14}$$

The non-dimensional downslope and normal components of the grain surface traction (2.19) are

$$-\varepsilon \hat{\sigma}_{xx}^e \frac{\partial \hat{s}^g}{\partial \hat{x}} + \mu \hat{\sigma}_{xz}^e = 0, \quad \hat{z} = \hat{s}^g(\hat{x}, \hat{t}), \tag{3.15}$$

$$-\varepsilon \mu \hat{\sigma}_{xz}^e \frac{\partial \hat{s}^g}{\partial \hat{x}} + \hat{\sigma}_{zz}^e = 0, \quad \hat{z} = \hat{s}^g(\hat{x}, \hat{t}), \tag{3.16}$$

and the non-dimensional components of the water surface traction (2.20) are

$$\varepsilon \phi^w \hat{p}^{w\star} \frac{\partial \hat{s}^w}{\partial \hat{x}} - \varepsilon^2 \hat{\tau}_{xx}^w \frac{\partial \hat{s}^w}{\partial \hat{x}} + \hat{\tau}_{xz}^w = 0, \quad \hat{z} = \hat{s}^w(\hat{x}, \hat{t}), \tag{3.17}$$

$$-\phi^w \hat{p}^{w\star} - \varepsilon \hat{\tau}_{xz}^w \frac{\partial \hat{s}^w}{\partial \hat{x}} + \varepsilon \hat{\tau}_{zz}^w = 0, \quad \hat{z} = \hat{s}^w(\hat{x}, \hat{t}). \tag{3.18}$$

The downslope and normal components of the basal granular traction (2.21) are

$$-\varepsilon\hat{\sigma}^e_{xx}\frac{\partial\hat{b}}{\partial\hat{x}} + \mu\hat{\sigma}^e_{xz} = -(\boldsymbol{n}^b\cdot\hat{\boldsymbol{\sigma}}^e\boldsymbol{n}^b)\left(\frac{\hat{u}^g_b}{|\hat{\boldsymbol{u}}^g_b|}\mu^b|\boldsymbol{\nabla}F^b| + \varepsilon\frac{\partial\hat{b}}{\partial\hat{x}}\right), \quad \hat{z} = \hat{b}(\hat{x}), \qquad (3.19)$$

$$-\varepsilon\mu\hat{\sigma}^e_{zx}\frac{\partial\hat{b}}{\partial\hat{x}} + \hat{\sigma}^e_{zz} = -(\boldsymbol{n}^b\cdot\hat{\boldsymbol{\sigma}}^e\boldsymbol{n}^b)\left(\varepsilon\frac{\hat{w}^g_b}{|\hat{\boldsymbol{u}}^g_b|}\mu^b|\boldsymbol{\nabla}F^b| - 1\right), \quad \hat{z} = \hat{b}(\hat{x}), \qquad (3.20)$$

where $|\hat{\boldsymbol{u}}^g_b| = \sqrt{(\hat{u}^g_b)^2 + \varepsilon^2(\hat{w}^g_b)^2}$ and $|\boldsymbol{\nabla}F^b| = \sqrt{1 + \varepsilon^2(\partial\hat{b}/\partial\hat{x})^2}$. Similarly, the downslope and normal components of the water basal friction (2.22) are

$$-\varepsilon^2\hat{\tau}^w_{xx}\frac{\partial\hat{b}}{\partial\hat{x}} + \hat{\tau}^w_{xz} + \varepsilon\left(\phi^w\hat{p}^{w\star}_b + (\boldsymbol{n}^b\cdot\hat{\boldsymbol{\sigma}}^w\boldsymbol{n}^b)\right)\frac{\partial\hat{b}}{\partial\hat{x}} = C^w\hat{u}^w|\hat{\boldsymbol{u}}^w|\|\boldsymbol{\nabla}F^b|, \quad \hat{z} = \hat{b}(\hat{x}), \quad (3.21)$$

$$-\varepsilon\hat{\tau}^w_{zx}\frac{\partial\hat{b}}{\partial\hat{x}} + \varepsilon\hat{\tau}^w_{zz} - \left(\phi^w\hat{p}^{w\star}_b + (\boldsymbol{n}^b\cdot\hat{\boldsymbol{\sigma}}^w\boldsymbol{n}^b)\right) = \varepsilon C^w\hat{w}^w|\hat{\boldsymbol{u}}^w|\|\boldsymbol{\nabla}F^b|, \quad \hat{z} = \hat{b}(\hat{x}), \quad (3.22)$$

where $|\hat{\boldsymbol{u}}^w| = \sqrt{(\hat{u}^w)^2 + \varepsilon^2(\hat{w}^w)^2}$.

4. Depth integration

4.1. *Depth-averaged mass balance equations*

The mass balance equations (3.2) and (3.6) can be integrated through the flow depth using Leibniz's rule (Abramowitz & Stegun 1970) to exchange the order of differentiation and integration, and then simplified by using the kinematic conditions (3.9)–(3.12). In the oversaturated regime, the standard argument (Savage & Hutter 1989; Gray *et al.* 1999) is complicated by the jump in the water volume fraction at the internal free surface of the grains. To overcome this, the integration of (3.6) is divided into two parts, which implies that the depth-integrated water mass balance is

$$\frac{\partial}{\partial\hat{t}}(\hat{h}^w\bar{\phi}^w) + \frac{\partial}{\partial\hat{x}}(\hat{h}^w\overline{\phi^w\hat{u}^w}) + \left[\!\left[\phi^w\left(\frac{\partial\hat{s}^g}{\partial\hat{t}} + \hat{u}^w\frac{\partial\hat{s}^g}{\partial\hat{x}} - \hat{w}^w\right)\right]\!\right] = 0, \qquad (4.1)$$

where the jump bracket is evaluated at $\hat{z} = \hat{s}^g$, the water thickness $\hat{h}^w = \hat{s}^w - \hat{b}$, and the depth-averaged water concentration and depth-averaged water flux are

$$\bar{\phi}^w = \frac{1}{\hat{h}^w}\int_{\hat{b}}^{\hat{s}^w}\phi^w d\hat{z}, \quad \overline{\phi^w\hat{u}^w} = \frac{1}{\hat{h}^w}\int_{\hat{b}}^{\hat{s}^w}\phi^w\hat{u}^w d\hat{z}, \qquad (4.2a,b)$$

respectively. The jump bracketed term in (4.1) is zero by the water mass jump condition (3.14), so the depth-averaged water mass balance reduces to standard form, despite the jump in concentration. A similar argument carries through in the same way for the depth-averaged grain mass balance in the undersaturated regime. As a result, the

depth-averaged grain and water mass balances are

$$\frac{\partial}{\partial \hat{t}}(\hat{h}^g \bar{\phi}^g) + \frac{\partial}{\partial \hat{x}}(\hat{h}^g \overline{\phi^g \hat{u}^g}) = 0, \tag{4.3}$$

$$\frac{\partial}{\partial \hat{t}}(\hat{h}^w \bar{\phi}^w) + \frac{\partial}{\partial \hat{x}}(\hat{h}^w \overline{\phi^w \hat{u}^w}) = 0, \tag{4.4}$$

where the granular flow thickness $\hat{h}^g = \hat{s}^g - \hat{b}$ and

$$\bar{\phi}^g = \frac{1}{\hat{h}^g} \int_{\hat{b}}^{\hat{s}^g} \phi^g \, d\hat{z}, \quad \overline{\phi^g \hat{u}^g} = \frac{1}{\hat{h}^g} \int_{\hat{b}}^{\hat{s}^g} \phi^g \hat{u}^g \, d\hat{z}. \tag{4.5a,b}$$

To further simplify (4.3) and (4.4), the vertical distributions of the solid and water volume fractions must be prescribed. The simplest approach is to assume that ϕ^g is constant, regardless of whether the flow is undersaturated or oversaturated, i.e.

$$\phi^g = \phi^c. \tag{4.6}$$

This is assumed in early debris flow models (Iverson 1997; Iverson & Denlinger 2001) and appears to be a good approximation in high solids volume fraction granular-dominated flows (Maurin *et al.* 2016; Chassagne *et al.* 2020). However, when the fluid can suspend grains, the solids volume fraction increases with depth (Egashira, Itoh & Takeuchi 2001; Maurin *et al.* 2016) and this will not be a good approximation. The fact that ϕ^c is constant and uniform throughout the debris flow precludes pore pressure effects (Iverson & George 2014). There is therefore potential to improve the model (at this point) in future. The exclusion of pore pressure effects does, however, allow us to show that they are not necessarily needed to drive the forward motion of grains from an oversaturated tail towards the flow front, which is the traditional view in the debris flow community.

As sketched in figure 2(*b,c*) the volume fraction of water is assumed to have a vertical distribution that is dependent on whether the flow is undersaturated or oversaturated. In the undersaturated regime,

$$\phi^w = \begin{cases} 0, & \hat{z} \in [\hat{s}^w, \hat{s}^g], \\ 1 - \phi^c, & \hat{z} \in [\hat{b}, \hat{s}^w], \end{cases} \tag{4.7}$$

while in the oversaturated regime,

$$\phi^w = \begin{cases} 1, & \hat{z} \in [\hat{s}^g, \hat{s}^w], \\ 1 - \phi^c, & \hat{z} \in [\hat{b}, \hat{s}^g]. \end{cases} \tag{4.8}$$

It is useful to define volume-fraction-weighted depth-averaged velocities

$$\hat{\bar{u}}^g = \frac{\displaystyle\int_{\hat{b}}^{\hat{s}^g} \phi^g \hat{u}^g \, d\hat{z}}{\displaystyle\int_{\hat{b}}^{\hat{s}^g} \phi^g \, d\hat{z}} = \frac{\overline{\phi^g \hat{u}^g}}{\bar{\phi}^g}, \quad \hat{\bar{u}}^w = \frac{\displaystyle\int_{\hat{b}}^{\hat{s}^w} \phi^w \hat{u}^w \, d\hat{z}}{\displaystyle\int_{\hat{b}}^{\hat{s}^w} \phi^w \, d\hat{z}} = \frac{\overline{\phi^w \hat{u}^w}}{\bar{\phi}^w}. \tag{4.9a,b}$$

Since the solids volume fraction is constant, (4.9*a*) reduces to the standard definition (Savage & Hutter 1989; Gray *et al.* 1999; Pitman & Le 2005; Gray & Edwards 2014). This is also true for the water in the undersaturated regime, but in the oversaturated regime, the internal concentration discontinuity (4.8) implies that the definition of the depth-averaged water velocity (4.9*b*) is different. Using the definitions (4.6)–(4.9*a,b*), it follows that the

depth-averaged mass balance of the grains in both the undersaturated and oversaturated regimes is

$$\frac{\partial}{\partial \hat{t}}(\hat{h}^g \phi^c) + \frac{\partial}{\partial \hat{x}}(\hat{h}^g \phi^c \hat{\bar{u}}^g) = 0, \tag{4.10}$$

while the depth-averaged mass balances for the water in the undersaturated and oversaturated regimes are

$$\frac{\partial}{\partial \hat{t}}(\hat{h}^w (1 - \phi^c)) + \frac{\partial}{\partial \hat{x}}(\hat{h}^w (1 - \phi^c) \hat{\bar{u}}^w) = 0, \tag{4.11}$$

$$\frac{\partial}{\partial \hat{t}}(\hat{h}^w (1 - \phi^c \hat{h}^g / \hat{h}^w)) + \frac{\partial}{\partial \hat{x}}(\hat{h}^w (1 - \phi^c \hat{h}^g / \hat{h}^w) \hat{\bar{u}}^w) = 0, \tag{4.12}$$

respectively. The factors ϕ^c and $1 - \phi^c$ in (4.10) and (4.11) are constants that could be cancelled out. However, these factors are retained here to develop a theoretical framework that can switch seamlessly between regimes.

4.2. *Normal components of the momentum equations*

The normal components of the momentum balances play a crucial role in deriving normal stresses in depth-averaged models (Savage & Hutter 1989; Iverson & Denlinger 2001; Gray & Edwards 2014). To leading order in ε, the water normal momentum balance (3.8) implies that the fluid pressure is hydrostatic

$$\frac{\partial \hat{p}^{w\star}}{\partial \hat{z}} = -\cos \zeta, \tag{4.13}$$

in both the mixed (ii) and pure water (iii) regions shown in figure 2(*b*,*c*). Excess pore pressure, which is important in large-scale debris flows containing fine particles (Iverson *et al.* 2010), is therefore neglected in this model. In the dry region (i), the water pressure and the Darcy drag vanish, and to leading order, the dry grain normal momentum balance (3.4) reduces to

$$\frac{\partial \hat{\sigma}_{zz}^e}{\partial \hat{z}} = -\phi^c \cos \zeta, \tag{4.14}$$

while in the mixed region (ii), the saturated grain normal stress gradient balances gravity and buoyancy

$$\frac{\partial \hat{\sigma}_{zz}^e}{\partial \hat{z}} = -\phi^c \cos \zeta - \gamma \phi^c \frac{\partial \hat{p}^{w\star}}{\partial \hat{z}}. \tag{4.15}$$

Equations (4.13)–(4.15), together with their respective boundary conditions, enable expressions for the pore fluid pressure and the grain normal stress to be derived, as presented below.

4.3. *Undersaturated pore fluid pressure and grain normal stress*

To leading order, the surface condition (3.18) reduces to

$$\hat{p}^{w\star}(\hat{s}^w) = 0. \tag{4.16}$$

The integration of (4.13) subject to (4.16) implies that the water pressure is hydrostatic

$$\hat{p}^{w\star} = (\hat{s}^w - \hat{z}) \cos \zeta, \quad \hat{z} \in [\hat{b}, \hat{s}^w]. \tag{4.17}$$

It follows that the pore fluid pressure on the base is

$$\hat{p}_b^{w\star} = \hat{h}^w \cos \zeta, \tag{4.18}$$

and that the depth-averaged water pressure is

$$\bar{\hat{p}}^{w\star} = \frac{1}{\hat{h}^w} \int_{\hat{b}}^{\hat{s}^w} \hat{p}^{w\star} \, d\hat{z} = \frac{1}{2} \hat{h}^w \cos \zeta. \tag{4.19}$$

To leading order, the grain surface condition (3.16) implies that the surface stress $\hat{\sigma}_{zz}^e$ vanishes. It follows that integrating (4.14) implies that the perpendicular grain normal stress in the dry region (i) is

$$\hat{\sigma}_{zz}^e = (\hat{s}^g - \hat{z})\phi^c \cos \zeta, \quad \hat{z} \in [\hat{s}^w, \hat{s}^g], \tag{4.20}$$

and hence that the perpendicular grain normal stress in the upper side of the water surface is $\hat{\sigma}_{zz}^{e+} = (\hat{s}^g - \hat{s}^w)\phi^c \cos \zeta$. Appendix A shows that provided the granular velocity profile through the depth of the flow is continuous, then there is no jump in the normal effective stress, and hence

$$\hat{\sigma}_{zz}^{e-} = \hat{\sigma}_{zz}^{e+} = (\hat{s}^g - \hat{s}^w)\phi^c \cos \zeta, \quad \hat{z} = \hat{s}^w. \tag{4.21}$$

In the saturated regime (ii), substitution of (4.13) into (4.15) implies that

$$\frac{\partial \hat{\sigma}_{zz}^e}{\partial \hat{z}} = -\phi^c (1 - \gamma) \cos \zeta, \quad \hat{z} \in [\hat{b}, \hat{s}^w]. \tag{4.22}$$

Integration of (4.22) subject to the continuity condition (4.21) implies that the perpendicular grain normal stress in the saturated regime (ii) is

$$\hat{\sigma}_{zz}^e = (\hat{s}^g - \hat{z})\phi^c \cos \zeta - (\hat{s}^w - \hat{z})\gamma \phi^c \cos \zeta, \quad \hat{z} \in [\hat{b}, \hat{s}^w], \tag{4.23}$$

and hence on the base,

$$\hat{\sigma}_{zz}^e(b) = (\hat{h}^g - \gamma \hat{h}^w)\phi^c \cos \zeta, \quad \hat{z} = \hat{b}. \tag{4.24}$$

The depth-averaged perpendicular grain normal stress is

$$\bar{\hat{\sigma}}_{zz}^e = \frac{1}{\hat{h}^g} \left(\int_{\hat{b}}^{\hat{s}^w} \hat{\sigma}_{zz}^e d\hat{z} + \int_{\hat{s}^w}^{\hat{s}^g} \hat{\sigma}_{zz}^e \, d\hat{z} \right) = \frac{1}{2} \hat{h}^g \phi^c \cos \zeta - \frac{1}{2} \gamma (\hat{h}^w / \hat{h}^g)^2 \hat{h}^g \phi^c \cos \zeta, \tag{4.25}$$

which, provided the earth pressure coefficient is equal to unity (Savage & Hutter 1989; Gray *et al.* 1999; Pouliquen 1999*a*), implies that the depth-averaged downslope grain normal stress is

$$\bar{\hat{\sigma}}_{xx}^e = \tfrac{1}{2} \hat{h}^g \phi^c \cos \zeta - \tfrac{1}{2} \gamma (\hat{h}^w / \hat{h}^g)^2 \hat{h}^g \phi^c \cos \zeta. \tag{4.26}$$

It follows that to leading order, (3.20) implies that the basal normal stress

$$\boldsymbol{n}^b \cdot \hat{\boldsymbol{\sigma}}^e \boldsymbol{n}^b = \hat{\sigma}_{zz}^e(b) = \hat{h}^g (1 - \gamma \hat{h}^w / \hat{h}^g)\phi^c \cos \zeta, \quad \hat{z} = \hat{b}. \tag{4.27}$$

943 A19-14

4.4. *Oversaturated pore fluid pressure and grain normal stress*

Since (4.13) is independent of ϕ^w, it can be integrated in the same way as the undersaturated case to show that the pressure is hydrostatic

$$\hat{p}^{w\star} = (\hat{s}^w - \hat{z}) \cos \zeta. \tag{4.28}$$

Similarly, the basal water pressure and the depth-averaged water pressure are the same as the undersaturated case

$$\hat{p}_b^{w\star} = \hat{h}^w \cos \zeta, \quad \hat{\bar{p}}^{w\star} = \tfrac{1}{2} \hat{h}^w \cos \zeta, \tag{4.29a,b}$$

and the pore fluid pressure at the grain surface is

$$\hat{p}^{w\star}(\hat{s}^g) = (\hat{h}^w - \hat{h}^g) \cos \zeta, \quad \hat{z} = \hat{s}^g. \tag{4.30}$$

To leading order, the traction-free condition (3.16) reduces to $\hat{\sigma}_{zz}^e(\hat{s}^g) = 0$. Substituting the gradient of the pore fluid pressure (4.13) into (4.15) and then integrating implies the perpendicular grain normal stress is

$$\hat{\sigma}_{zz}^e = (1 - \gamma)(\hat{s}^g - \hat{z})\phi^c \cos \zeta, \quad \hat{z} \in [\hat{b}, \hat{s}^g], \tag{4.31}$$

and hence that the perpendicular basal normal stress is

$$\hat{\sigma}_{zz}^e(\hat{b}) = (1 - \gamma)\hat{h}^g \phi^c \cos \zeta \quad \hat{z} = \hat{b}. \tag{4.32}$$

The depth-averaged perpendicular normal stress is then

$$\hat{\bar{\sigma}}_{zz}^e = \frac{1}{\hat{h}^g} \int_{\hat{b}}^{\hat{s}^g} \hat{\sigma}_{zz}^e d\hat{z} = \frac{1}{2}(1 - \gamma)\hat{h}^g \phi^c \cos \zeta. \tag{4.33}$$

Given that the earth pressure coefficient is unity, the depth-averaged downslope normal stress is therefore equal to its counterpart in the vertical direction, i.e.

$$\hat{\bar{\sigma}}_{xx}^e = \tfrac{1}{2}(1 - \gamma)\hat{h}^g \phi^c \cos \zeta. \tag{4.34}$$

To leading order, (3.20) shows the basal normal stress

$$\boldsymbol{n}^b \cdot \hat{\boldsymbol{\sigma}}^e \boldsymbol{n}^b = \hat{\sigma}_{zz}^e(\hat{b}) = (1 - \gamma)\hat{h}^g \phi^c \cos \zeta. \tag{4.35}$$

4.5. *Undersaturated depth-averaged downslope momentum balances*

The downslope grain momentum balance (3.3) is now integrated from the bed $\hat{z} = \hat{b}$ to the grain surface $\hat{z} = \hat{s}^g$. The integration is divided into two parts, because the buoyancy and Darcy drag are active only below the water surface $\hat{z} = \hat{s}^w$. Leibniz's integration rule is used to swap the order of differentiation and integration, and the surface and basal kinematic conditions, (3.9) and (3.10), and downslope surface traction (3.15) are used to simplify the resulting equations. The calculations are lengthy and are therefore shown in

Appendix B. The resulting depth-averaged momentum balance for the grains is

$$
\varepsilon \left(\frac{\partial}{\partial \hat{t}} (\hat{h}^g \overline{\phi^g \hat{u}^g}) + \frac{\partial}{\partial \hat{x}} (\hat{h}^g \overline{\phi^g (\hat{u}^g)^2}) + \frac{\partial}{\partial \hat{x}} (\hat{h}^g \hat{\bar{\sigma}}_{xx}^e) + \gamma \phi^c \frac{\partial}{\partial \hat{x}} (\hat{h}^w \hat{\bar{p}}^w) \right)
$$

$$
= \hat{h}^g \phi^c \sin \zeta - \left(\varepsilon \hat{\sigma}_{xx}^e(\hat{b}) \frac{\partial \hat{b}}{\partial \hat{x}} - \mu \hat{\sigma}_{xz}^e(\hat{b}) \right) - \gamma \hat{C}^d \int_{\hat{b}}^{\hat{s}^w} (\hat{u}^g - \hat{u}^w) \, d\hat{z} - \varepsilon \gamma \phi^c \hat{p}_b^{w\star} \frac{\partial \hat{b}}{\partial \hat{x}}.
\tag{4.36}
$$

Substituting (4.27) into (3.19) implies that the basal downslope traction

$$
\varepsilon \hat{\sigma}_{xx}^e(\hat{b}) \frac{\partial \hat{b}}{\partial \hat{x}} - \mu \hat{\sigma}_{xz}^e(\hat{b}) = \frac{\hat{u}_b^g}{|\hat{u}_b^g|} (1 - \gamma \hat{h}^w / \hat{h}^g) \mu^b \hat{h}^g \phi^c \cos \zeta
$$

$$
+ \varepsilon (1 - \gamma \hat{h}^w / \hat{h}^g) \hat{h}^g \phi^c \cos \zeta \frac{\partial \hat{b}}{\partial \hat{x}} + O(\varepsilon^2),
\tag{4.37}
$$

where the factor $\hat{u}_b^g / |\hat{u}_b^g|$ will be approximated as $\hat{\bar{u}}^g / |\hat{\bar{u}}^g|$. This approximation is employed in virtually all depth-averaged granular flow models (see e.g. Savage & Hutter 1989; Pitman & Le 2005; Pudasaini 2012; Gray & Edwards 2014; Iverson & George 2014). To simplify the momentum transport terms, it is assumed that

$$
\overline{\phi^g (\hat{u}^g)^2} = \frac{1}{\hat{h}^g} \int_{\hat{b}}^{\hat{s}^g} \phi^g (\hat{u}^g)^2 \, d\hat{z} = \chi^g \bar{\phi}^g (\hat{\bar{u}}^g)^2,
\tag{4.38}
$$

where the shape factor χ^g for specific velocity profiles will be considered in § 4.8. It is also useful to define the streamfunction for the grains

$$
\hat{\psi}^g(\hat{z}) = \int_{\hat{b}}^{\hat{z}} \hat{u}^g(\hat{z}') \, d\hat{z}',
\tag{4.39}
$$

which allows the Darcy drag exerted on the grain phase to be expressed as

$$
\gamma \hat{C}^d \int_{\hat{b}}^{\hat{s}^w} (\hat{u}^g - \hat{u}^w) \, d\hat{z} = \gamma \hat{C}^d (\hat{\psi}^g(\hat{s}^w) - \hat{h}^w \hat{\bar{u}}^w).
\tag{4.40}
$$

The gravitational force, the basal friction and the Darcy drag are all order unity quantities, but their sum is an order ε quantity. To express this theoretically, the leading order balance $\hat{\mathcal{L}}^g$ is defined as

$$
\varepsilon \hat{\mathcal{L}}^g = \underbrace{\hat{h}^g \phi^c \sin \zeta}_{Gravity} - \underbrace{\mu^b \frac{\hat{\bar{u}}^g}{|\hat{\bar{u}}^g|} \left(1 - \gamma \frac{\hat{h}^w}{\hat{h}^g} \right) \hat{h}^g \phi^c \cos \zeta}_{Basal \ friction} - \underbrace{\gamma \hat{C}^d (\hat{\psi}^g(\hat{s}^w) - \hat{h}^w \hat{\bar{u}}^w)}_{Darcy \ drag}.
\tag{4.41}
$$

When (4.6), (4.9a), (4.37), (4.38) and (4.41) are substituted into (4.36), together with the basal pressure (4.18), the depth-averaged pore fluid pressure (4.19) and the depth-averaged normal stress (4.26), the leading-order depth-averaged grain momentum balance in the

943 A19-16

undersaturated regime becomes

$$\frac{\partial}{\partial \hat{t}}(\hat{h}^g \phi^c \hat{\bar{u}}^g) + \frac{\partial}{\partial \hat{x}}\left(\chi^g \hat{h}^g \phi^c (\hat{\bar{u}}^g)^2 + \frac{1}{2}(\hat{h}^g)^2 \phi^c \cos \zeta - \frac{1}{2}\gamma (\hat{h}^w)^2 \phi^c \cos \zeta\right) = \hat{S}^g, \quad (4.42)$$

where the source terms

$$\hat{S}^g = \hat{\mathcal{L}}^g - \underbrace{\gamma \hat{h}^w \phi^c \cos \zeta \frac{\partial \hat{h}^w}{\partial \hat{x}}}_{Buoyancy} - \underbrace{\hat{h}^g \phi^c \cos \zeta \frac{\partial \hat{b}}{\partial \hat{x}}}_{Topographic\ gradient}, \quad (4.43)$$

combine the leading order balance (4.41) with the lower order buoyancy and topographic gradient terms. Note that the gradient of $(1/2)\gamma(\hat{h}^w)^2 \phi^c \cos \zeta$ in (4.42) can be cancelled with the buoyancy term in (4.43). However, the equations are left in their present form to unify all the regimes in § 4.7.

Integrating the downslope water momentum balance (3.7) from the bed $\hat{z} = \hat{b}$ to the water surface $\hat{z} = \hat{s}^w$ is more straightforward, because the integration does not pass through a singular surface. Using Leibniz's integration rule to exchange the order of differentiation and integration and using the kinematic conditions (3.11) and (3.12), the surface traction (3.17) and the Darcy drag (4.40), the depth-averaged downslope water momentum balance is

$$\varepsilon \left(\frac{\partial}{\partial \hat{t}}(\hat{h}^w (1 - \phi^c) \hat{\bar{u}}^w) + \frac{\partial}{\partial \hat{x}}(\chi^w \hat{h}^w (1 - \phi^c)(\hat{\bar{u}}^w)^2) + (1 - \phi^c)\frac{\partial}{\partial \hat{x}}(\hat{h}^w \hat{\bar{p}}^{w\star})\right)$$

$$- \varepsilon^2 \frac{\partial}{\partial \hat{x}}(\hat{h}^w \hat{\bar{\tau}}_{xx}^w) = \hat{h}^w (1 - \phi^c) \sin \zeta - \hat{C}^d (\hat{h}^w \hat{\bar{u}}^w - \hat{\psi}^g(\hat{s}^w)) - \varepsilon (1 - \phi^c) \hat{p}_b^{w\star} \frac{\partial \hat{b}}{\partial \hat{x}}$$

$$+ \left(\varepsilon^2 \hat{\tau}_{xx}^w(\hat{b})\frac{\partial \hat{b}}{\partial \hat{x}} - \hat{\tau}_{xz}^w(\hat{b})\right), \quad (4.44)$$

where the water shape factor χ^w is defined as

$$\overline{\phi^w (\hat{u}^w)^2} = \frac{1}{\hat{h}^w}\int_{\hat{b}}^{\hat{s}^w} \phi^w (\hat{u}^w)^2 \, d\hat{z} = \chi^w \bar{\phi}^w (\hat{\bar{u}}^w)^2. \quad (4.45)$$

The depth-averaged in-plane viscous stress $\hat{\bar{\tau}}_{xx}^w$ is smaller than the other forces, and is usually neglected (Savage & Hutter 1989; Pitman & Le 2005). However, it plays a crucial role in some subtle situations, including (i) obtaining the correct cutoff frequency of roll waves (Forterre 2006; Gray & Edwards 2014), (ii) generating cross-stream velocity profiles (Iverson & Denlinger 2001; Baker, Johnson & Gray 2016*b*; Meng & Wang 2018), (iii) regularising ill-posedness (Baker *et al.* 2016*a*) and (iv) forming critical phenomena like levees (Rocha, Johnson & Gray 2019). An expression for the depth-averaged in-plane deviatoric water stresses in the undersaturated regime is derived in Appendix C. A similar depth-averaged in-plane viscous-like term, analogous to that derived by Gray & Edwards (2014), could also be added to (4.43). However, both these terms are small, and are not important for reproducing the experimental observations of Davies (1988, 1990) in § 5.

To leading order, (3.22) reduces to

$$\boldsymbol{n}^b \cdot \hat{\boldsymbol{\sigma}}^w \boldsymbol{n}^b = -\phi^w \hat{p}_b^{w\star}, \tag{4.46}$$

and together with (3.21), it shows

$$-\varepsilon^2 \hat{\tau}_{xx}^w(\hat{b}) \frac{\partial \hat{b}}{\partial \hat{x}} + \hat{\tau}_{xz}^w(\hat{b}) = C^w \hat{\bar{u}}^w |\hat{\bar{u}}^w| + O(\varepsilon^2). \tag{4.47}$$

In an analogous way to the grain phase, the sum of the gravitational force, the Chézy drag and the Darcy drag is small, although they are all individually order unity quantities. To express this mathematically, the leading order balance $\hat{\mathcal{L}}^w$ is defined as

$$\varepsilon \hat{\mathcal{L}}^w = \underbrace{\hat{h}^w (1 - \phi^c) \sin \zeta}_{Gravity} - \underbrace{C^w \hat{\bar{u}}^w |\hat{\bar{u}}^w|}_{Chézy\ drag} - \underbrace{\hat{C}^d (\hat{h}^w \hat{\bar{u}}^w - \hat{\psi}^g(\hat{s}^w))}_{Darcy\ drag}. \tag{4.48}$$

When (4.45) and (4.48) are substituted into (4.44), together with the basal pressure (4.18), the depth-averaged pore fluid pressure (4.19) and the depth-averaged shear stress (C3), the leading-order water momentum balance in the undersaturated regime becomes

$$\frac{\partial}{\partial \hat{t}} (\hat{h}^w (1 - \phi^c) \hat{\bar{u}}^w) + \frac{\partial}{\partial \hat{x}} \left(\chi^w \hat{h}^w (1 - \phi^c) (\hat{\bar{u}}^w)^2 + \frac{1}{2} (\hat{h}^w)^2 \cos \zeta \right) = \hat{S}^w, \tag{4.49}$$

where the source term

$$\hat{S}^w = \hat{\mathcal{L}}^w + \underbrace{\phi^c \hat{h}^w \cos \zeta \frac{\partial \hat{h}^w}{\partial \hat{x}}}_{Buoyancy} - \underbrace{\hat{h}^w (1 - \phi^c) \cos \zeta \frac{\partial \hat{b}}{\partial \hat{x}}}_{Topographic\ gradient} + \underbrace{\frac{2\varepsilon}{Re} \frac{\partial}{\partial \hat{x}} \left(\hat{h}^w (1 - \phi^c) \frac{\partial \hat{\bar{u}}^w}{\partial \hat{x}} \right)}_{Viscous\ term}, \tag{4.50}$$

combines the leading order balance (4.48) with the lower order buoyancy, topography gradient and viscous terms.

4.6. *Oversaturated depth-averaged downslope momentum balances*

It is also straightforward to integrate the downslope granular momentum balance (3.3) from $\hat{z} = \hat{b}$ to the grain surface $\hat{z} = \hat{s}^g$, since there is no singular surface. By using Leibniz's integration rule to exchange the order of differentiation and integration, together with the surface and basal kinematic conditions (3.9) and (3.10), the depth-averaged downslope granular momentum balance in the oversaturated region is

$$\varepsilon \left(\frac{\partial}{\partial \hat{t}} (\hat{h}^g \phi^c \hat{\bar{u}}^g) + \frac{\partial}{\partial \hat{x}} (\chi^g \hat{h}^g \phi^c (\hat{\bar{u}}^g)^2) + \frac{\partial}{\partial \hat{x}} (\hat{h}^g \hat{\bar{\sigma}}_{xx}^e) + \gamma \phi^c \frac{\partial}{\partial \hat{x}} \left(\int_{\hat{b}}^{\hat{s}^g} \hat{p}^{w\star} d\hat{z} \right) \right)$$

$$= \hat{h}^g \phi^c \sin \zeta - \left(\varepsilon \hat{\sigma}_{xx}^e(\hat{b}) \frac{\partial \hat{b}}{\partial \hat{x}} - \mu \hat{\sigma}_{xz}^e(\hat{b}) \right) - \gamma \hat{C}^d \int_{\hat{b}}^{\hat{s}^g} (\hat{u}^g - \hat{u}^w) \, d\hat{z}$$

$$+ \varepsilon \gamma \phi^c \left(\hat{p}^{w\star} \frac{\partial \hat{z}}{\partial \hat{x}} \right)_{\hat{b}}^{\hat{s}^g}, \tag{4.51}$$

where the basal granular traction is determined by the downslope component of the basal friction condition (3.19) and the basal normal stress (4.35), i.e.

$$\varepsilon \hat{\sigma}_{xx}^e \frac{\partial \hat{b}}{\partial \hat{x}} - \mu \hat{\sigma}_{xz}^e = \mu^b \frac{\hat{\bar{u}}^g}{|\hat{\bar{u}}^g|} (1 - \gamma) \hat{h}^g \phi^c \cos \zeta + \varepsilon (1 - \gamma) \hat{h}^g \phi^c \cos \zeta \frac{\partial \hat{b}}{\partial \hat{x}} + O(\varepsilon^2). \tag{4.52}$$

This time, it is useful to define the streamfunction for the water

$$\hat{\psi}^w(\hat{z}) = \int_{\hat{b}}^{\hat{z}} \hat{u}^w(\hat{z}') \, d\hat{z}', \tag{4.53}$$

which allows the Darcy drag to be expressed as

$$\gamma \hat{C}^d \int_{\hat{b}}^{\hat{s}^g} (\hat{u}^g - \hat{u}^w) \, d\hat{z} = \gamma \hat{C}^d (\hat{h}^g \bar{\hat{u}}^g - \hat{\psi}^w(\hat{s}^g)). \tag{4.54}$$

The difference of the gravitational force, the basal friction and the Darcy drag is of order ε. This leading order balance is expressed mathematically by defining the function

$$\varepsilon \hat{\mathcal{L}}^g = \underbrace{\hat{h}^g \phi^c \sin \zeta}_{Gravity} - \underbrace{\mu^b \frac{\bar{\hat{u}}^g}{|\bar{\hat{u}}^g|}(1-\gamma)\hat{h}^g \phi^c \cos \zeta}_{Basal\ friction} - \underbrace{\gamma \hat{C}^d (\hat{h}^g \bar{\hat{u}}^g - \hat{\psi}^w(\hat{s}^g))}_{Darcy\ drag}. \tag{4.55}$$

Substituting the hydrostatic water pressure (4.28) into the relevant terms in (4.51) implies that

$$-\frac{\partial}{\partial \hat{x}} \left(\int_{\hat{b}}^{\hat{s}^g} \hat{p}^{w\star} \, d\hat{z} \right) + \left(\hat{p}^{w\star} \frac{\partial \hat{z}}{\partial \hat{x}} \right)_{\hat{b}}^{\hat{s}^g} = -\hat{h}^g \cos \zeta \frac{\partial \hat{h}^w}{\partial \hat{x}} - \hat{h}^g \cos \zeta \frac{\partial \hat{b}}{\partial \hat{x}}. \tag{4.56}$$

Finally, substituting (4.54)–(4.56) together with the depth-averaged downslope normal stress (4.34) into (4.51) implies that the depth-averaged granular momentum balance is

$$\frac{\partial}{\partial \hat{t}}(\hat{h}^g \phi^c \bar{\hat{u}}^g) + \frac{\partial}{\partial \hat{x}} \left(\chi^g \hat{h}^g \phi^c (\bar{\hat{u}}^g)^2 + \frac{1}{2}(\hat{h}^g)^2 (1-\gamma)\phi^c \cos \zeta \right) = \hat{S}^g, \tag{4.57}$$

where the source term $\hat{S}^g$ on the right-hand side is

$$\hat{S}^g = \hat{\mathcal{L}}^g - \underbrace{\gamma \hat{h}^g \phi^c \cos \zeta \frac{\partial \hat{h}^w}{\partial \hat{x}}}_{Buoyancy} - \underbrace{\hat{h}^g \phi^c \cos \zeta \frac{\partial \hat{b}}{\partial \hat{x}}}_{Topographic\ gradient}. \tag{4.58}$$

To leading order, the normal component of the Chézy formula (3.22) reduces to

$$\mathbf{n}^b \cdot \hat{\boldsymbol{\sigma}}^w \mathbf{n}^b = -\phi^w \hat{p}_b^{w\star}, \tag{4.59}$$

which implies the downslope component of the Chézy formula (3.21) becomes

$$-\varepsilon^2 \hat{\tau}_{xx}^w(\hat{b}) \frac{\partial \hat{b}}{\partial \hat{x}} + \hat{\tau}_{xz}^w(\hat{b}) = C^w \bar{\hat{u}}^w |\bar{\hat{u}}^w| + O(\varepsilon^2). \tag{4.60}$$

In the oversaturated region, the water volume fraction is discontinuous across the grain free surface, so the integral of the downslope component of the water momentum balance (3.7) through the water depth is complicated. The detailed derivation can be found in

[Appendix D.]{.underline} It follows from this calculation that the depth-integrated water momentum balance in the oversaturated regime is

$$\varepsilon \left(\frac{\partial}{\partial \hat{t}}((\hat{h}^w - \phi^c \hat{h}^g)\hat{\bar{u}}^w) + \frac{\partial}{\partial \hat{x}}(\chi^w(\hat{h}^w - \phi^c \hat{h}^g)(\hat{\bar{u}}^w)^2) + \frac{\partial}{\partial \hat{x}}(\hat{h}^w \hat{\bar{p}}^{w\star}) - \varepsilon \frac{\partial}{\partial \hat{x}}(\hat{h}^w \hat{\bar{\tau}}^w_{xx}) \right)$$

$$= (\hat{h}^w - \phi^c \hat{h}^g) \sin \zeta - C^w \hat{\bar{u}}^w |\hat{\bar{u}}^w| - \hat{C}^d(\hat{\psi}^w(\hat{s}^g) - \hat{h}^g \hat{\bar{u}}^g) + \varepsilon \left(\hat{p}^{w\star} \frac{\partial \hat{z}}{\partial \hat{x}} \right)^{\hat{s}^w}_{\hat{b}}$$

$$+ \varepsilon \phi^c \frac{\partial}{\partial \hat{x}} \left(\int_{\hat{b}}^{\hat{s}^g} \hat{p}^{w\star} \, d\hat{z} \right) - \varepsilon \phi^c \left(\hat{p}^{w\star} \frac{\partial \hat{z}}{\partial \hat{x}} \right)^{\hat{s}^g}_{\hat{b}}. \tag{4.61}$$

This time, the leading order balance lies between the gravitational force, the Chézy drag and the Darcy drag. The sum of these terms is of order ε, which is expressed mathematically by defining the function

$$\varepsilon \hat{\mathcal{L}}^w = \underbrace{(\hat{h}^w - \phi^c \hat{h}^g) \sin \zeta}_{Gravity} - \underbrace{C^w \hat{\bar{u}}^w |\hat{\bar{u}}^w|}_{Chézy\ drag} - \underbrace{\hat{C}^d(\hat{\psi}^w(\hat{s}^g) - \hat{h}^g \hat{\bar{u}}^g)}_{Darcy\ drag}. \tag{4.62}$$

Using (4.16), (4.29*a,b*), (4.56), (4.62) and the depth-averaged shear stress (C4), the leading-order depth-averaged oversaturated water momentum balance becomes

$$\frac{\partial}{\partial \hat{t}}((\hat{h}^w - \phi^c \hat{h}^g)\hat{\bar{u}}^w) + \frac{\partial}{\partial \hat{x}} \left(\chi^w(\hat{h}^w - \phi^c \hat{h}^g)(\hat{\bar{u}}^w)^2 + \frac{1}{2}(\hat{h}^w)^2 \cos \zeta \right) = \hat{S}^w, \tag{4.63}$$

where the source term

$$\hat{S}^w = \hat{\mathcal{L}}^w + \underbrace{\hat{h}^g \phi^c \cos \zeta \frac{\partial \hat{h}^w}{\partial \hat{x}}}_{Buoyancy} - \underbrace{(\hat{h}^w - \phi^c \hat{h}^g) \cos \zeta \frac{\partial \hat{b}}{\partial \hat{x}}}_{Topographic\ gradient} + \underbrace{\frac{2\varepsilon}{Re} \frac{\partial}{\partial \hat{x}} \left((\hat{h}^w - \phi^c \hat{h}^g) \frac{\partial \hat{\bar{u}}^w}{\partial \hat{x}} \right)}_{Viscous\ term}.$$

$$\tag{4.64}$$

4.7. *Unified dimensional system of depth-averaged equations*

The leading-order system (4.10), (4.11), (4.42) and (4.49) in the undersaturated regime, and (4.10), (4.12), (4.57) and (4.63) in the oversaturated regime can be made dimensional by reversing the scalings

$$x = L\hat{x}, \quad (h^v, s^v, b) = H(\hat{h}^v, \hat{s}^v, \hat{b}), \quad t = (L/\sqrt{gH})\hat{t}, \quad u^v = \sqrt{gH}\hat{u}^v,$$
$$\left. (S^v, \mathcal{L}^v) = (gH^2/L)(\hat{S}^v, \hat{\mathcal{L}}^v), \quad C^d = (\varrho^{w\star}\sqrt{g}/\sqrt{H})\hat{C}^d, \quad \psi^v = H\sqrt{gH}\hat{\psi}^v. \right\}$$

$$\tag{4.65a–g}$$

They can also be written in a unified form by introducing the variable

$$\mathcal{H} = \min(h^w, h^g)/h^w, \tag{4.66}$$

which determines the proportion of the water height that is occupied by grains. As shown in figure 2(*b,c*), this implies that

$$\mathcal{H} = \begin{cases} 1, & h^g > h^w, \quad \text{(undersaturated)}, \\ h^g/h^w, & h^g \le h^w, \quad \text{(oversaturated)}. \end{cases} \tag{4.67}$$

It follows that the unified system of dimensional equations can be expressed as

$$\frac{\partial}{\partial t}(h^g \phi^c) + \frac{\partial}{\partial x}(h^g \phi^c \bar{u}^g) = 0, \tag{4.68}$$

$$\frac{\partial}{\partial t}(h^w (1 - \phi^c \mathcal{H})) + \frac{\partial}{\partial x}(h^w (1 - \phi^c \mathcal{H}) \bar{u}^w) = 0, \tag{4.69}$$

$$\frac{\partial}{\partial t}(h^g \phi^c \bar{u}^g) + \frac{\partial}{\partial x}\left(\chi^g h^g \phi^c (\bar{u}^g)^2 + \frac{1}{2}(h^g)^2 \phi^c g \cos \zeta - \frac{1}{2}\gamma \phi^c (h^w \mathcal{H})^2 g \cos \zeta\right) = S^g, \tag{4.70}$$

$$\frac{\partial}{\partial t}(h^w (1 - \phi^c \mathcal{H}) \bar{u}^w) + \frac{\partial}{\partial x}\left(\chi^w h^w (1 - \phi^c \mathcal{H})(\bar{u}^w)^2 + \frac{1}{2}(h^w)^2 g \cos \zeta\right) = S^w, \tag{4.71}$$

where the terms on the left-hand side of (4.70) and (4.71) represent the momentum transport and pressure gradients of each phase. The source terms on the right-hand side of (4.70) and (4.71) take the form

$$S^g = \mathcal{L}^g - \underbrace{\gamma \phi^c \mathcal{H} h^w g \cos \zeta \frac{\partial h^w}{\partial x}}_{\text{Buoyancy}} - \underbrace{h^g \phi^c g \cos \zeta \frac{\partial b}{\partial x}}_{\text{Topography gradient}}, \tag{4.72}$$

$$S^w = \mathcal{L}^w + \underbrace{\phi^c \mathcal{H} h^w g \cos \zeta \frac{\partial h^w}{\partial x}}_{\text{Buoyancy}} - \underbrace{(1 - \phi^c \mathcal{H}) h^w g \cos \zeta \frac{\partial b}{\partial x}}_{\text{Topography gradient}}$$

$$+ \underbrace{2\nu^w \frac{\partial}{\partial x}\left(h^w (1 - \phi^c \mathcal{H}) \frac{\partial \bar{u}^w}{\partial x}\right)}_{\text{Viscous term}}, \tag{4.73}$$

where the kinematic viscosity of water

$$\nu^w = \eta^w / \varrho^{w\star}. \tag{4.74}$$

The dimensional leading order balances are

$$\mathcal{L}^g = \underbrace{h^g \phi^c g \sin \zeta}_{\text{Gravity}} - \underbrace{\frac{\bar{u}^g}{|\bar{u}^g|}\left(1 - \gamma \mathcal{H}\frac{h^w}{h^g}\right) \mu^b h^g \phi^c g \cos \zeta}_{\text{Basal friction}} + \underbrace{\frac{C^d}{\varrho^{g\star}}\left(\psi^w(s^v) - \psi^g(s^v)\right)}_{\text{Darcy drag}}, \tag{4.75}$$

$$\mathcal{L}^w = \underbrace{h^w (1 - \phi^c \mathcal{H}) g \sin \zeta}_{\text{Gravity}} - \underbrace{C^w \bar{u}^w |\bar{u}^w|}_{\text{Basal friction}} - \underbrace{\frac{C^d}{\varrho^{w\star}}\left(\psi^w(s^v) - \psi^g(s^v)\right)}_{\text{Darcy drag}}, \tag{4.76}$$

where the internal interface height in the Darcy drag terms is defined as

$$s^v = \mathcal{H}h^w + b = \begin{cases} s^w, & h^g > h^w, \quad \text{(undersaturated)}, \\ s^g, & h^g \leq h^w, \quad \text{(oversaturated)}. \end{cases} \tag{4.77}$$

Equations (4.66)–(4.77) provide a convenient way of expressing the equations in all four regimes shown in figure 2, i.e. the dry granular front, the undersaturated region, the

oversaturated region and the watery tail. In the undersaturated regime, the buoyancy terms in (4.72) and (4.73) can be written in conservative form. In this case, the whole system is in conservative form, which is advantageous for numerical methods (Kurganov & Tadmor 2000) as well as for deriving jump conditions (Chadwick 1976) at internal shocks. In the oversaturated regime, the buoyancy terms can not be written in conservative form, which is potentially a problem for numerical methods and if shocks develop. However, the presence of the viscous term in (4.73) will suppress the formation of water shocks, since the higher order gradient terms will smooth out any discontinuities. If granular shocks develop during oversaturated flows, it may also be necessary to add a viscous term to the depth-averaged granular momentum balance (see e.g. Gray & Edwards 2014).

4.8. *Velocity profiles through the flow depth*

To evaluate the shape factors in (4.70) and (4.71) and the Darcy drag terms in (4.75) and (4.76), it is necessary to make some assumptions about the velocity profiles through the depth of grains and the water. These assumptions must take account of the layered structure of the flow (4.6)–(4.8) in the undersaturated and oversaturated regimes (figure 2), and be consistent with the definitions of the depth-averaged velocities in (4.9a,b). This paper introduces shear into the model by defining the velocity for phase ν of the form

$$u^\nu = u_c^\nu(x, t) \left(\alpha^\nu + 2(1 - \alpha^\nu) \left(\frac{z - b}{h^\nu} \right) \right), \tag{4.78}$$

where u_c^ν is independent of z and the parameter $\alpha^\nu \in [0, 1]$ allows the velocity profile to vary from simple shear with no basal slip ($\alpha^\nu = 0$) to plug flow ($\alpha^\nu = 1$) (Gray & Thornton 2005; Gray & Kokelaar 2010; Johnson *et al.* 2012). It would also be possible to use a power law or a Bagnold velocity profile (Turnbull, Bowman & McElwaine 2015; Baker *et al.* 2016b). The shear velocity profile (4.78) contrasts with widely used debris-flow models (e.g. Iverson & Denlinger 2001; Pitman & Le 2005; Pelanti, Bouchut & Mangeney 2008; Pudasaini 2012; Iverson & George 2014; Meng & Wang 2016), which assume plug flow for both the grain and water phases.

This paper will show that velocity shear is sufficient to produce a dry granular front without the need to invoke ideas about particle segregation (Iverson 2003; Gray 2018). Consider then the linear velocity profiles with depth given by (4.78). Since the volume fraction of grains is always equal to the constant ϕ^c by (4.6), and the volume fraction of water is equal to the constant $1 - \phi^c$ in the undersaturated regime (4.7), it follows from (4.9a,b) that

$$u_c^g = \bar{u}^g, \quad u_c^w = \bar{u}^w. \tag{4.79a,b}$$

The corresponding granular and water shape factors, defined in (4.38) and (4.45), are

$$\chi^g = \tfrac{4}{3} - \tfrac{2}{3}\alpha^g + \tfrac{1}{3}(\alpha^g)^2, \quad \chi^w = \tfrac{4}{3} - \tfrac{2}{3}\alpha^w + \tfrac{1}{3}(\alpha^w)^2, \tag{4.80a,b}$$

respectively. For these cases, the shape factor $\chi^\nu = 1$ for plug flow and 4/3 for simple shear. The situation for the oversaturated regime is more complex, because the volume fraction of water (4.8) is also height dependent. Substituting (4.8) and (4.78) into (4.9b)

943 A19-22

implies that

$$u_c^w = \lambda^w \bar{u}^w, \tag{4.81}$$

where

$$\lambda^w = \frac{(1 - \phi^c \mathcal{H})}{1 - \phi^c(\alpha^w \mathcal{H} + (1 - \alpha^w)\mathcal{H}^2)}. \tag{4.82}$$

Note that when $\mathcal{H} = 1$, $\lambda^w = 1$ and (4.81) reduces to the undersaturated case. Solving (4.45) for the shape factor and substituting the depth-averaged water velocity (4.9b) implies that

$$\chi^w = \frac{\overline{\phi^w(u^w)^2}\bar{\phi}^w}{(\overline{\phi^w u^w})^2}. \tag{4.83}$$

The oversaturated water shape factor is therefore

$$\chi^w = \frac{(4\chi_0^w - 2\chi_1^w \alpha^w + \chi_2^w(\alpha^w)^2)(1 - \mathcal{H}\phi^c)}{3(1 - \phi^c(\alpha^w \mathcal{H} + (1 - \alpha^w)\mathcal{H}^2))^2}, \tag{4.84}$$

where the coefficients

$$\left.\begin{aligned}\chi_0^w &= 1 - \mathcal{H}^3\phi^c, \quad \chi_1^w = 1 + 3\mathcal{H}^2\phi^c - 4\mathcal{H}^3\phi^c,\\ \chi_2^w &= 1 - 3\mathcal{H}\phi^c + 6\mathcal{H}^2\phi^c - 4\mathcal{H}^3\phi^c.\end{aligned}\right\} \tag{4.85a–c}$$

Thus, (4.84) reduces to the undersaturated case (4.80b) when $\mathcal{H} = 1$. For the velocity profiles (4.78), it follows from the definitions of the streamfunctions (4.39) and (4.53) that in the undersaturated regime,

$$\psi^w(s^w) - \psi^g(s^w) = h^w \bar{u}^w - \bar{u}^g \left(\alpha^g h^w + (1 - \alpha^g)\frac{(h^w)^2}{h^g}\right). \tag{4.86}$$

Similarly, in the oversaturated regime at the internal grain surface,

$$\psi^w(s^g) - \psi^g(s^g) = \lambda^w \bar{u}^w \left(\alpha^w h^g + (1 - \alpha^w)\frac{(h^g)^2}{h^w}\right) - h^g \bar{u}^g, \tag{4.87}$$

where the factor λ^w enters due to the non-uniform concentration of water with z. This paper investigates the simplest possible shearing debris flow model, by assuming simple shear in the granular phase and plug flow in the water, i.e.

$$\alpha^g = 0, \quad \text{and} \quad \alpha^w = 1. \tag{4.88a,b}$$

With these assumptions, it follows from (4.86) and (4.87) that the difference of the streamfunctions, which arises in (4.75) and (4.76), can be expressed in the unified form

$$\psi^w(s^v) - \psi^g(s^v) = h^w \mathcal{H} \bar{u}^w - \frac{(h^w \mathcal{H})^2}{h^g} \bar{u}^g. \tag{4.89}$$

The assumption of plug flow in the water implies that $\chi^w = 1$, and for simplicity, it is further assumed that the grain shape factor $\chi^g = 1$, which is a common assumption in depth-averaged debris flow models (e.g. Iverson & Denlinger 2001; Pitman & Le 2005; Pelanti *et al.* 2008; Pudasaini 2012; Iverson & George 2014; Meng & Wang 2016).

943 A19-23

4.9. *Closure of friction coefficients μ^b and C^w*

Considerable progress has been made in the field of the granular flows with the development of $\mu(I)$-rheology (GDR-MiDi 2004; Jop, Forterre & Pouliquen 2006), where the friction coefficient μ is a monotonically increasing function of inertial number I. This functional dependence was determined from measurements of steady-uniform flows between the angles ζ_1 and ζ_2 on an inclined plane (Pouliquen 1999*b*; Pouliquen & Forterre 2002). The ensuing empirical friction law is given by

$$\mu^b(Fr, h^g) = \mu_1 + \frac{\mu_2 - \mu_1}{1 + \dfrac{\beta h^g}{\mathscr{L} Fr}}, \qquad (4.90)$$

where $\mu_1 = \tan \zeta_1$ and $\mu_2 = \tan \zeta_2$. The parameter β is an empirical constant and $\mathscr{L}$ has the dimensions of a length and is dependent on the properties of the grains and on the bed roughness. The Froude number in (4.90) is defined as

$$Fr = \frac{|\bar{u}^g|}{\sqrt{h^g g \cos \zeta}}. \qquad (4.91)$$

Maurin *et al.* (2016) used a coupled fluid–discrete-element method to perform numerical simulations of turbulent bedload transport. Contrary to expectations, they found that for dense submerged granular flows, the effect of the interstitial fluid viscosity was negligible. Moreover, they found that the $\mu(I)$-rheology was able to collapse the simulated shear-to-normal stress ratio and the solids volume fraction over an unexpectedly wide range of inertial numbers. This lends weight to the use of the granular friction (4.90) to describe the basal friction of the grains. It enters the theory through the leading order granular source term defined in (4.75), which includes a factor $1 - \gamma \mathcal{H} h^w / h^g$ to account for the reduced granular normal stress in the submerged grains.

The water bed friction coefficient is based on the Manning equation (Manning 1891; Chaudhry 2008) for open channel flows, which implies that $C^w = gn^2/(h^w)^{1/3}$, where n is the Manning coefficient (Chertock *et al.* 2015). This formula is modified to account for the presence of grains by defining it to be

$$C^w = (1 - \phi^c \mathcal{H}) \frac{gn^2}{(h^w)^{1/3}}. \qquad (4.92)$$

This ensures that C^w reduces to the classical form for shallow water flows in the absence of grains.

5. Davies' moving bed flume experiments

Davies (1988, 1990) generated small-scale steady-state flows on a moving conveyor belt that possess many features in common with geophysical flows in the field, e.g. dry snouts and pure watery tails. Davies' carefully described experiments (figure 3 and online supplementary movies 2–4) are a good test of the present theory because the moving conveyor belt reduces the average bulk flow speed to zero, allowing detailed study of the shear profiles and relative motion between grains and fluid that remain. They have also been used by Berzi & Jenkins (2009) to test against their steady-state kinetic theory based debris flow model.
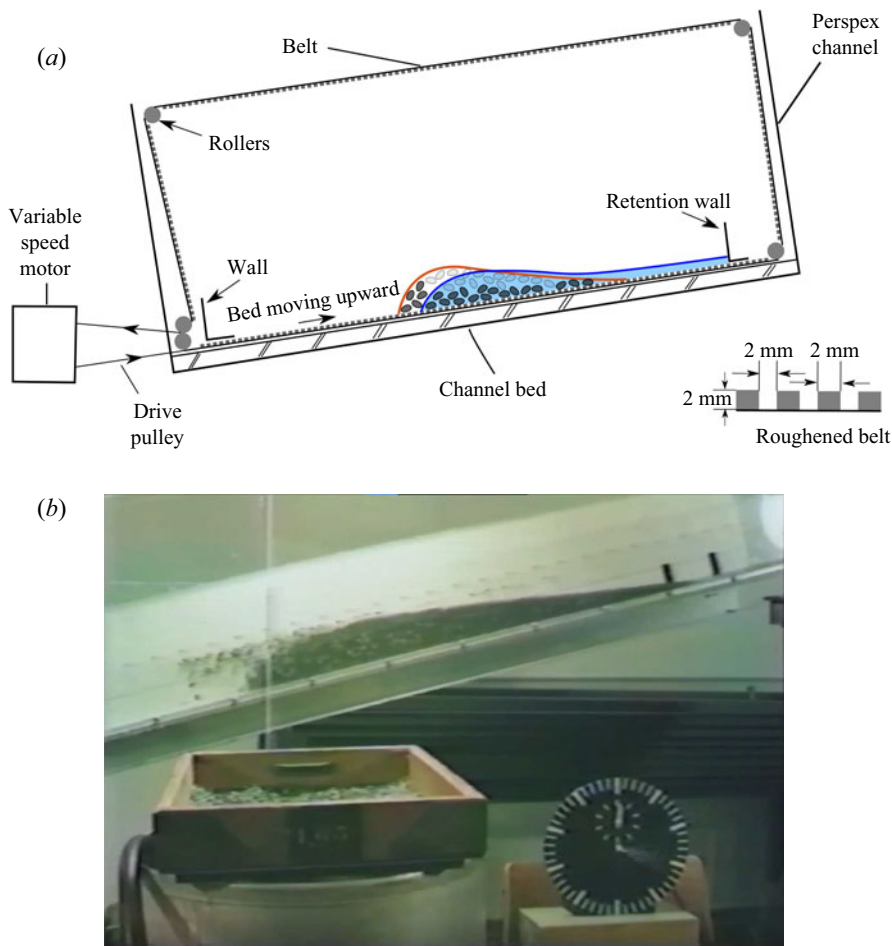
Figure 3. (*a*) Schematic diagrams of Davies' (1988) moving bed flume experiment and the toothed belt. (*b*) A photo of the experiment on a 15° slope and with a bed speed $U = 0.3\,\mathrm{m\,s}^{-1}$. Three movies of the experiment are available in the online supplementary material (courtesy of Davies 1988, 1990).

5.1. *Description and summary of observations*

The moving-bed apparatus consisted of a rectangular flume that was 2 m in length and had a width of 50 mm, with walls at the ends to retain all the material, see figure 3. The channel bed was made rough by using a corrugated nylon belt, driven by a toothed drive wheel connected by another toothed belt to a variable-speed electric motor and controller. The range of channel slopes used in the experiments was from 5° to 19° and the bed speeds ranged from 0.25 to 1.17 m s^{-1}. Room temperature tap water was used and the plastic grains were 4-mm-long cylinders cut from 4-mm diameter polyvinyl chloride (PVC) rod with intrinsic density $\varrho^{g\star} = 1400\,\mathrm{kg\,m}^{-3}$. The maximum grain volume fraction was 0.56. Approximately 10 % of the particles were painted white to act as tracers, and videos were used to track individual particle paths. In Davies' (1988) experiments, the surge remains stationary, while the bed moves upward at a constant velocity U. The main experimental findings relevant to the current study are outlined below.

(i) Adding grains caused the flow depth to increase and a curved front appeared in the channel. As more grains were added, and the grain volume exceeded the threshold for uniform flow at a given speed and slope angle, the excess grains moved to the front and caused a thicker dry snout to develop. This dry bulbous flow head is similar in form to those observed in large scale debris flows.

(ii) As more grains were added, a substantial high-concentration stationary surge was formed at the lower end of the channel. This surge had a uniform depth body that extended from the curved front to an attenuated tail. The depth of this uniform body was not very sensitive to the grain volume, as shown in figure 9 of Davies (1990). The flows usually formed on a relatively gentle slope or when the bed speed was relatively low. An example is shown in online supplementary movie 2, at a slope angle of $15°$ and bed speed $U = 0.2\,\mathrm{m\,s}^{-1}$.

(iii) When the bed speed was raised to a relatively high value, the stationary surge was curved rather than being of uniform depth (see e.g. online supplementary movie 3 at $15°$ inclination and bed speed $U = 0.3\,\mathrm{m\,s}^{-1}$). The longitudinal profiles showed that a dry front is followed by an undersaturated and oversaturated body that degenerates down to pure water in the tail, as sketched in figure 2. This longitudinal profile is similar to those observed in the USGS debris-flow flume tests (Iverson *et al.* 2010; Johnson *et al.* 2012) and in the small scale experimental curved channel of Scheidl *et al.* (2015).

(iv) Tracers show that grains near the free surface are sheared towards the front, are overrun there and transported back towards the tail near the base of the flow. Here they rise up to the surface again and are sheared forward to form a recirculating cell that conserves its mass.

5.2. *Experimental parameters*

Davies (1988) provided the values of the slope angle ζ, the solids volume fraction ϕ^c, the density ratio γ, the particle diameter d and the water viscosity η^w. These experimental parameters are summarised in table 1. At the time, the $\mu(I)$-rheology had not been developed, so exact values of the parameters in the friction law (4.90) were not determined. However, Armanini *et al.* (2005) has conducted experiments using similar plastic cylinders, and Berzi & Jenkins (2008) show that these cylinders are more frictional than glass beads (Pouliquen 1999b), but less frictional than sand. The values of ζ_1 and ζ_2 are therefore assumed to be slightly larger than those for glass beads presented in table I of Pouliquen (1999b). The value of β follows from Pouliquen (1999b) and Gray & Edwards (2014). The measurements of Forterre & Pouliquen (2003) show that the frictional length scale $\mathscr{L}$ depends on the grain diameter d, and that it is approximately equal to $1.65d$ for glass beads in dry granular flows. The parameters measured for dry flows are adopted here without modification. However, it should be noted that the basal friction in (4.75) includes a factor $1 - \gamma \mathcal{H} h^w / h^g$ to account for the reduced granular normal stress when the grains are submerged in water. This is consistent with Maurin *et al.* (2016) who measured quite large shear-to-normal stress ratios in their coupled fluid-discrete-element method simulations of bed load transport.

The steady-uniform water flow at the tail in Davies' (1988) experiments implies a balance between the gravitational force and the Chézy friction in (4.76),

$$h_0^w g \sin \zeta = g n^2 (\bar{u}_0^w)^2 / (h_0^w)^{1/3}, \tag{5.1}$$

Parameter	Measured values	Model values
Solids volume fraction, ϕ^c	0.56	0.56
Diameter, d	4 mm	4 mm
Water density, $\varrho^{w\star}$	tap water	$1000 \, \text{kg m}^{-3}$
Water viscosity, η^w	tap water	$0.001 \, \text{Pa s}$
Solids density, $\varrho^{g\star}$	$1400 \, \text{kg m}^{-3}$	$1400 \, \text{kg m}^{-3}$
Manning's coefficient, n	—	$0.0593 \, \text{s m}^{-(1/3)}$
Minimum bed friction angle, ζ_1	—	$24.57°$
Maximum bed friction angle, ζ_2	—	$36.5°$
Empirical flow rule parameter, β	—	0.135
Frictional length scale, $\mathscr{L}$	—	$1.65 \times d$

Table 1. Physical parameters in the experiments and the computation.

where h_0^w and $\bar{u}_0^w$ are the steady-uniform thickness and speed of the bed, respectively. It follows that Manning's coefficient is

$$n = \sqrt{\frac{(h_0^w)^{4/3} \sin \zeta}{(\bar{u}_0^w)^2}}. \tag{5.2}$$

For Davies' (1988) experiment shown in the online supplementary material (movie 4), the slope inclination angle $\zeta = 19°$, the bed speed $\bar{u}_0^w = 0.3 \, \text{m s}^{-1}$ and the steady-uniform water depth in the tail lies between one- and two-grain diameters. Assuming $h_0^w = 5.5 \, \text{mm}$, Manning's coefficient is $n = 0.0593 \, \text{s m}^{-(1/3)}$. All these additional parameters are also summarised in table 1. In particular, none of them are fitting parameters.

6. Steady travelling wave solutions

Davies' (1988, 1990) moving bed flume experiments develop steady travelling states that are similar to flow fronts observed in the field (Pierson 1986). This section investigates whether the governing equations, summarised in § 4.7, can also support such travelling wave solutions, and explain the formation of dry snouts (Hungr 2000; Berzi & Jenkins 2008; Leonardi *et al.* 2015).

6.1. *Case 1: formation of bulbous heads in the undersaturated regime*

The online supplementary movie of Davies' (1988, 1990) experiment shows that when the bed speed is relatively small, a dry bulbous head develops that is connected to an undersaturated body of approximately constant depth. This configuration is equivalent to the case where the surge is steadily translating on an unmoved bed. It is therefore useful to transform the governing equations (4.68)–(4.71) into a frame of reference moving with speed U, by making the coordinate transformation

$$\xi = x - Ut, \quad \tau = t. \tag{6.1a,b}$$

943 A19-27

The steady-state grain and water mass balances in the moving frame are therefore

$$\frac{\mathrm{d}}{\mathrm{d}\xi}(h^g \phi^c (\bar{u}^g - U)) = 0, \tag{6.2}$$

$$\frac{\mathrm{d}}{\mathrm{d}\xi}(h^w (1 - \phi^c \mathcal{H})(\bar{u}^w - U)) = 0, \tag{6.3}$$

respectively. Integrating (6.2) and (6.3), subject to the condition that $h^g = 0$ and $h^w = 0$ at the front, implies that

$$h^g \phi^c (\bar{u}^g - U) = 0, \quad h^w (1 - \phi^c \mathcal{H})(\bar{u}^w - U) = 0. \tag{6.4a,b}$$

These are satisfied either when h^g or h^w are identically zero, or when

$$\bar{u}^g = \bar{u}^w = U, \tag{6.5}$$

i.e. the depth-averaged velocities of the grains and the water are equal to the moving frame speed.

Since the depth-averaged water velocity is independent of ξ and $b = 0$ in Davies' (1988, 1990) experiments, the viscous term and the topography gradients vanish in the source terms (4.72)–(4.73). Assuming that the flow is undersaturated ($\mathcal{H} = 1$) and that $\chi^v = 1$, the steady-state depth-averaged momentum balances (4.70)–(4.71) in the travelling frame reduce to

$$h^g \phi^c (\bar{u}^g - U)\frac{\mathrm{d}\bar{u}^g}{\mathrm{d}\xi} + h^g \phi^c g \cos \zeta \frac{\mathrm{d}h^g}{\mathrm{d}\xi} = h^g \phi^c g \sin \zeta$$

$$- \mu^b h^g \phi^c g \cos \zeta (1 - \gamma h^w/h^g) + \frac{180\eta^w h^w (\phi^c)^2}{\varrho^{g\star}(1 - \phi^c)d^2}(\bar{u}^w - \bar{u}^g h^w/h^g), \tag{6.6}$$

$$h^w (1 - \phi^c)(\bar{u}^w - U)\frac{\mathrm{d}\bar{u}^w}{\mathrm{d}\xi} + h^w (1 - \phi^c) g \cos \zeta \frac{\mathrm{d}h^w}{\mathrm{d}\xi} = h^w (1 - \phi^c) g \sin \zeta$$

$$- (1 - \phi^c) g (n\bar{u}^w)^2/(h^w)^{1/3} - \frac{180\eta^w h^w (\phi^c)^2}{\varrho^{w\star}(1 - \phi^c)d^2}(\bar{u}^w - \bar{u}^g h^w/h^g), \tag{6.7}$$

where it is implicitly assumed that the sidewall friction in Davies' (1988, 1990) experiments is sufficiently small that this one-dimensional theory can be applied.

Using (6.5) to eliminate $\bar{u}^g$ and $\bar{u}^w$ in favour of U, it follows that (6.6) and (6.7) reduce to a pair of ordinary differential equations (ODEs) for the thicknesses h^g and h^w

$$\frac{\mathrm{d}h^g}{\mathrm{d}\xi} = \tan \zeta - \mu^b (1 - \gamma h^w/h^g) + \frac{180\eta^w \phi^c}{\varrho^{g\star} g \cos \zeta (1 - \phi^c)d^2}\frac{h^w}{h^g}(1 - h^w/h^g)U, \tag{6.8}$$

$$\frac{\mathrm{d}h^w}{\mathrm{d}\xi} = \tan \zeta - (nU)^2/((h^w)^{4/3} \cos \zeta) - \frac{180\eta^w (\phi^c)^2}{\varrho^{w\star} g \cos \zeta (1 - \phi^c)^2 d^2}(1 - h^w/h^g)U. \tag{6.9}$$

The grain thickness gradient in (6.8) is balanced by gravity, the buoyancy-reduced friction and the Darcy drag, while the water thickness gradient in (6.9) balances gravity, the Chézy drag and the Darcy drag.

In a dry snout, the position of the grain front ξ_f^g lies further downslope than the water front ξ_f^w, and within this region, the water depth h^w vanishes. As a result, (6.8) reduces to

$$\frac{\mathrm{d}h^g}{\mathrm{d}\xi} = \tan \zeta - \mu^b. \tag{6.10}$$

This equation was originally derived by Pouliquen (1999a) to compute the shape of a dry granular front, and admits an exact solution (Gray & Ancey 2009) for the friction law

943 A19-28

(4.90). As $h^w \to 0$, the Chézy drag is singular in the water ODE (6.9). It follows that at the water front, the dominant balance is between the thickness gradient and Chézy drag, i.e.

$$\frac{\mathrm{d}h^w}{\mathrm{d}\xi} = -\frac{(nU)^2}{(h^w)^{4/3} \cos \zeta}. \tag{6.11}$$

Integrating (6.11) subject to the condition that $h^w = 0$ at $\xi = \xi_f^w$, implies that

$$h^w = \left[\frac{7}{3} \frac{(nU)^2}{\cos \zeta} (\xi_f^w - \xi) \right]^{3/7}, \tag{6.12}$$

which determines the water free surface in the neighbourhood of the front.

Without loss of generality, the granular front is assumed to lie at $\xi_f^g = 0$, and (6.10) is integrated upstream using Matlab's ode45 initial value problem solver to determine h^g. This solution is valid until the water front is reached at $\xi = \xi_f^w$, which is a free parameter in the problem. The approximate solution (6.12) is used to determine the water surface for small h^w, and then the ODEs (6.8) and (6.9) are integrated upstream to determine both h^w and h^g. Figure 4 shows two solution profiles for a 15° slope and a bed speed $U = 0.262 \,\mathrm{m\,s}^{-1}$. In figure 4(*a*), the dry front is assumed to be 18 grain diameters long, and both the water and grain fronts are connected to the far field steady states by monotonically decreasing curves. Such solutions resemble those of monodisperse dry granular flows (Pouliquen 1999*a*), and agree with the experimental observation of Davies (1988) that for low speed flows on shallow inclines, the dry snout is connected to an upstream uniform-depth undersaturated flow. Although the depth-averaged velocities of grains and water are equal, the local velocities are not. In the lower, saturated part of the flow, the water flows downslope more quickly than the grains, and helps to drag the granular phase downslope. In the upper unsaturated part of the flow, velocity shear results in the grains (alone) being transported downslope faster than either the water or grains in the lower saturated part of the flow. This differs from the model of Berzi *et al.* (2010), in which the local grain and water velocities are assumed to be equal in the steady uniform flow far upstream of the front. This results in their solutions approaching an exactly saturated state $h^w = h^g$ upstream.

When the dry front is doubled in length, to $\xi_f^g - \xi_f^w = 36$ grain diameters (figure 4*b*), there is much more resistance from the dry snout, and the granular front has to have a steeper gradient to drive it downslope. As a result, both the granular and the water free surfaces develop a pronounced bulge just upstream of the bump, as shown in figure 4(*b*). In the dry snout, the component of gravitational acceleration is smaller than the basal friction, so that there is a negative thickness gradient. Upstream of the water front, the basal granular friction diminishes gradually, due to the buoyancy imparted by the interstitial fluid. This implies that the driving force gets close to the buoyancy-reduced grain friction, and exceeds it just upstream of the peak grain depth, implying the gradient of h^g is positive there. In the wet region, the driving force, i.e. the downslope component of gravitational acceleration, balances the resistance due to Chézy drag and the Darcy interaction force for the water phase. Near the water front, the water thickness is sufficiently thin that the Chézy drag outweighs the gravity-driven force, and a steep water front forms with a negative thickness gradient. Note that far upstream, the two solutions shown in figure 4(*a,b*) approach the same steady uniform states.
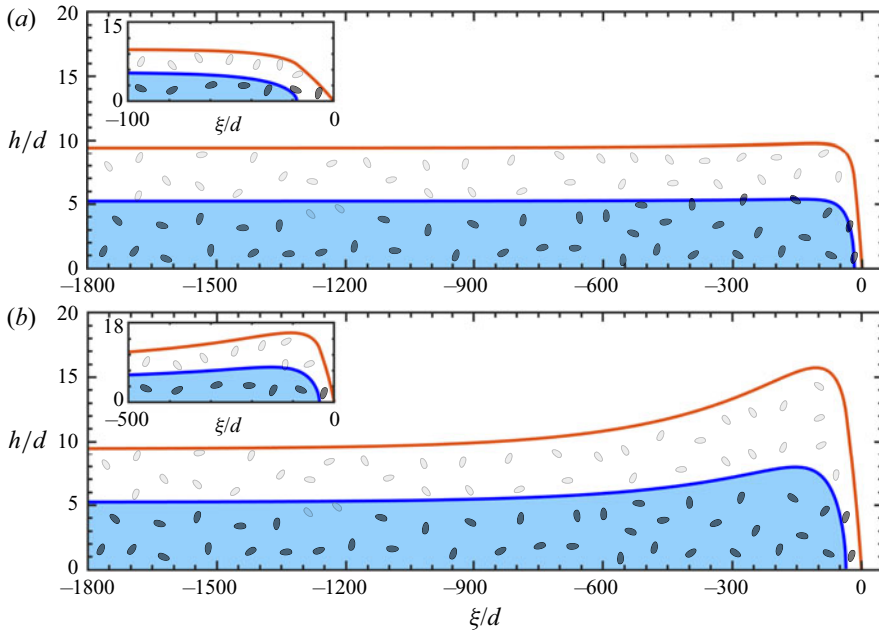
Figure 4. Longitudinal profiles of the grain depth (brown lines) and water depth (blue lines) with $\zeta = 15°$ and $U = 0.262 \, \text{m s}^{-1}$ for (*a*) $\xi_f^g - \xi_f^w = 18d$ and (*b*) $\xi_f^g - \xi_f^w = 36d$. The blue shaded regions represent water-saturated material and a few schematic grains are shown in the granular region to make it easier to identify. The flow direction is from left to right and the insets show a close-up view of the front.

6.2. *Case 2: formation of bulbous heads and pure watery tails*

When the bed speed U is increased, the granular free surface becomes more curved, as shown in the supplementary online movies 3 and 4 of Davies' (1988, 1990) experiments. As a result, the flow develops a dry snout, an undersaturated region that smoothly transitions into an oversaturated flow and then a watery tail, as shown schematically in figure 2. This is qualitatively different from the experiments and solutions described in § 6.1 for low bed speeds. In the travelling frame (6.1*a,b*), the steady-state mass balances (6.2) and (6.3), together with the grain and water free frontal condition, imply that either h^g and h^w are identically zero or the depth-averaged grain and water velocities are equal to the bed speed

$$\bar{u}^g = \bar{u}^w = U. \tag{6.13}$$

As in § 6.1, the solution starts at the front of the dry snout, which is assumed to lie at $\xi_f^g = 0$. The dry granular momentum balance (6.10) is then integrated back to the water front at ξ_f^w using Matlab's ode45 initial value solver. The approximate solution (6.12) at the water front is used to initiate the solution of the undersaturated ODEs (6.8) and (6.9). These are integrated upstream until the transition point is reached between the undersaturated and oversaturated regimes, where $h^g = h^w$. To advance the solution further, ODEs need to be derived for the oversaturated regime. Assuming that the shape factors χ^ν equal unity, the steady-state oversaturated depth-averaged momentum balances (4.70) and (4.71) in the

943 A19-30

travelling frame reduce to

$$h^g \phi^c (\bar{u}^g - U) \frac{\mathrm{d}\bar{u}^g}{\mathrm{d}\xi} + h^g (1 - \gamma) \phi^c g \cos \zeta \frac{\mathrm{d}h^g}{\mathrm{d}\xi} + \gamma h^g \phi^c g \cos \zeta \frac{\mathrm{d}h^w}{\mathrm{d}\xi} = h^g \phi^c g \sin \zeta$$

$$- \mu^b h^g \phi^c g \cos \zeta (1 - \gamma) + \frac{180 \eta^w h^g (\phi^c)^2}{\varrho^{g\star}(1 - \phi^c)d^2}(\bar{u}^w - \bar{u}^g), \tag{6.14}$$

$$(h^w - h^g \phi^c)(\bar{u}^w - U) \frac{\mathrm{d}\bar{u}^w}{\mathrm{d}\xi} + (h^w - h^g \phi^c) g \cos \zeta \frac{\mathrm{d}h^w}{\mathrm{d}\xi} = (h^w - h^g \phi^c) g \sin \zeta$$

$$- (h^w - h^g \phi^c) \frac{g(n\bar{u}^w)^2}{(h^w)^{4/3}} - \frac{180 \eta^w h^g (\phi^c)^2}{\varrho^{w\star}(1 - \phi^c)d^2}(\bar{u}^w - \bar{u}^g), \tag{6.15}$$

respectively. Substituting the velocity condition (6.13) into (6.14) and (6.15) eliminates the acceleration and Darcy drag terms, even though locally, the grains, water and moving frame are all moving at different speeds. The resulting pair of equations can be solved for the gradients of the grain and water thicknesses

$$\frac{\mathrm{d}h^g}{\mathrm{d}\xi} = \tan \zeta - \mu^b + \frac{\gamma}{1 - \gamma} \frac{(nU)^2}{(h^w)^{4/3} \cos \zeta}, \tag{6.16}$$

$$\frac{\mathrm{d}h^w}{\mathrm{d}\xi} = \tan \zeta - \frac{(nU)^2}{(h^w)^{4/3} \cos \zeta}. \tag{6.17}$$

The lubrication effect of the water phase on the grains is characterised by a buoyancy force that acts against the granular friction, and has the form of a Chézy drag. This is different from (6.8) in the undersaturated regime, where the lubrication effect is characterised by the buoyancy-reduced friction.

The ODEs (6.16) and (6.17) are integrated back from the transition point until h^g reaches zero at ξ_t^g. Since $h^g = 0$ is a trivial solution of (6.14), the underlying system naturally degenerates to a single ODE (6.17) that can be solved for the shape of the pure water tail, upstream of ξ_t^g. Figure 5 shows solutions for the free surfaces of the grains and the water at a slope angle $\zeta = 15°$, bed speed $U = 0.39 \,\mathrm{m\,s}^{-1}$ and for three values of the snout length $\xi_f^g - \xi_f^w$, which is a free parameter in the problem. Increasing the snout length results in an increase of the total volume of grains in the travelling wave. In the undersaturated regime, the water phase moves locally faster than the grains at the bottom of the flow, but slower than the dry surface grains, which are sheared forward to form the dry snout. In the oversaturated tail, the flow becomes sufficiently thin that the basal friction experienced by the water outweighs that acting on the grains. As a result, grains that reach the granular free surface are sheared forward to leave a watery upstream tail. This process can be seen in Davies' (1988) experimental movies 3 and 4 in the online supplementary material. The solutions in figure 5 illustrate that it is possible to model the forward motion of the grains relative to the water, without the need to invoke the traditional view (in the debris flow community) that excess pore pressures are needed to drive the forward motion of grains in the oversaturated tail.

For the solutions shown in figures 4 and 5, the snout length is the natural parameter to use when solving the ODEs, and the total volume of grains and water emerges as part of the solution. Conversely, in physical experiments, the total volume of grains and water is prescribed, and one then has to iterate on the snout length to select the solution with the correct water and grain volumes. Figure 5(b) shows a comparison of the computed grain free surface and that measured by Davies (1988) at the same bed speed and
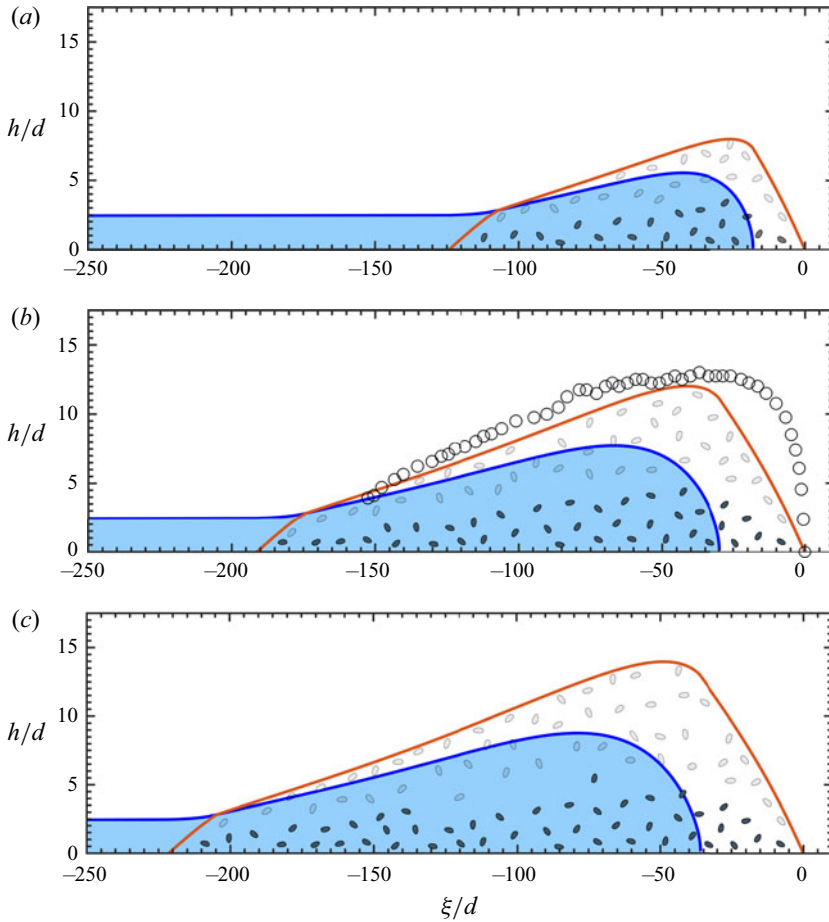
Figure 5. Longitudinal profiles of the grain depth (brown lines) and water depth (blue lines) with $\zeta = 15°$ and $U = 0.39\,\mathrm{m\,s^{-1}}$, for (a) $\xi_f^g - \xi_f^w = 18d$, (b) $\xi_f^g - \xi_f^w = 29.7485d$ and (c) $\xi_f^g - \xi_f^w = 36d$. The blue shaded regions represent water-saturated material and a few schematic grains are shown in the granular region to make it easier to identify. The '$\circ$' symbols in panel (b) represent the granular free surface measured by Davies (1990) at the same bed speed and inclination. The flow direction is from left to right.

slope angle. The computed amplitude, length and slope of the granular free surface in the tail are in good agreement with the experiments. The main deviation from the experimental measurements lies in the frontal profile, which may be due to a collisional shear layer that forms near the moving bed in the experiments. Detailed profiles of the water free surface are not reported in Davies (1988, 1990). However, Davies (1990) does say that the water free surface is approximately one-grain diameter below the granular free surface in the main part of the unsaturated body. Figure 5(b) shows that the water free surface lies within two grain diameters of the grain free surface for the majority of the undersaturated region. The theory therefore captures the key qualitative features of the flow as well as providing a good quantitative match to Davies' (1990) granular free surface data without any fitting parameters.

943 A19-32

6.3. *Recirculation of the grains*

In Davies' (1988) experiments, approximately 10 % of the grains were painted white to reveal the particle paths. This can also be simulated by reconstructing the two-dimensional velocity field from the depth-averaged velocity and tracing out the streamlines. It follows from (4.78), (4.79a,b) and (4.88a,b) that the downstream velocity of the grains is given by the linear shear profile

$$u^g = 2\bar{u}^g \left(\frac{z - b}{h^g} \right). \tag{6.18}$$

The granular mass balance (2.2) with the assumption of constant solids volume fraction (4.6) implies that in the moving frame, the grains satisfy bulk incompressibility

$$\frac{\partial u^g}{\partial \xi} + \frac{\partial w^g}{\partial z} = 0. \tag{6.19}$$

This can be integrated through the depth z, subject to the condition that $w^g = 0$ on the bottom $z = b$, to give the normal velocity

$$w^g = \frac{\bar{u}^g}{(h^g)^2} \frac{dh^g}{d\xi} (z - b)^2. \tag{6.20}$$

Following Gray & Ancey (2009), the particle paths in the moving frame

$$\frac{d\xi^p}{dt} = u^g - U, \quad \frac{dz^p}{dt} = w^g \tag{6.21a,b}$$

can be reconstructed by solving

$$\frac{dz^p}{d\xi} = \frac{w^g}{u^g - U}. \tag{6.22}$$

This can be simplified by introducing the streamfunction coordinate

$$\psi(\xi, z(\xi)) = \int_b^{z(\xi)} u^g(\xi, z') - U \, dz'. \tag{6.23}$$

Assuming that $\psi^p(\xi)$ is the particle path $z = z^p(\xi)$, Leibniz's rule can be used to swap the order of differentiation and integration in the derivative $d\psi^p/d\xi$, and hence, using the bulk incompressibility (6.19), the no normal velocity condition $w^g(b) = 0$ and (6.22), this implies

$$\frac{d\psi^p}{d\xi} = (u^g - U)\frac{dz^p}{d\xi} - w^g = 0. \tag{6.24}$$

The streamfunction is therefore constant along a given particle path. An explicit expression for ψ can be obtained by substituting the downstream velocity component (6.18) into (6.23) and recalling that the depth-averaged velocity $\bar{u}^g$ is equal to the bed speed U in the travelling wave solution (6.5), to give

$$\psi = \frac{(z - b)^2}{h^g} U - (z - b)U. \tag{6.25}$$

It follows that the streamfunction ψ equals zero on both the free surface $z = s^g$ and the base $z = b$. This implies that there is a closed streamline that runs along the grain free surface and base, which forms a recirculating cell. Grains on the free surface are sheared

towards the flow front, where they are over-run and remain stationary on the bottom while the flow passes over them. As the tail propagates past, these basal grains are picked up again and sheared towards the front.

Within the $\psi = 0$ contour, there are a nested set of recirculating closed particle paths, as shown in figure 6(*a*). At each ξ, the streamfunction reaches a local minimum $\psi_{min} = -h^g U/4$ at $z = z_{min} = b + h^g/2$. This is also the point where the downslope velocity (6.18) is equal to the frame speed U, i.e. it is the no-mean-flow line in the frame of the wave. Grains above the no-mean-flow line migrate towards the front and grains below advect backwards in the moving frame and are overtaken by the tail. An explicit relation for the particle paths can be obtained by solving the quadratic equation (6.25) for z to give

$$z = \begin{cases} b + \frac{1}{2}h^g + \frac{1}{2}\sqrt{(h^g)^2 + 4\psi h^g/U}, & z \geq z_{min}, \\ b + \frac{1}{2}h^g - \frac{1}{2}\sqrt{(h^g)^2 + 4\psi h^g/U}, & z < z_{min}. \end{cases} \quad (6.26)$$

The predicted grain paths (figure 6*c*) are in good agreement with Davies' (1990) measured particle paths over a one-second time interval (figure 6*b*). Both measurements and prediction show that grains near the surface are moving forward towards the front, while those near the base are transported backward (in the moving frame) and rise up again to prevent the surge from losing mass. This clearly indicates that strong shear develops in the flow. Some discrepancies also exist. This is largely because the velocity profile in Davies' (1990) experiments has the shear concentrated at the bottom of the flow and it is sheared less strongly near the free surface.

7. Conclusions

In this paper, a depth-averaged two-phase model is derived to account for the development of dry snouts and watery tails in granular–fluid mixtures, such as debris flows and lahars. Most of the existing depth-averaged models for debris flows assume that the flow is saturated and the contribution of the interstitial water is characterised by the bed pore fluid pressure that mitigates the bed granular friction (Iverson & George 2014), or by buoyancy and interaction drag forces that couple the grain and water phases (Pitman & Le 2005). These models usually solve for the mixture depth and solids volume fraction, in addition to the depth-averaged velocities. Since the water typically experiences less frictional resistance to motion than the grains, existing debris flow models predict that water moves to the flow front (e.g. see figure 3(*c*) in George & Iverson (2011) and figure 2 in Pudasaini 2012). As a result, the formation of dry snouts, observed in the field (Pierson 1986) and in large scale debris experiments (Iverson 2003; Iverson *et al.* 2010; Johnson *et al.* 2012), is often attributed to particle-size segregation.

The laboratory experiment of Davies (1988, 1990) show that the formation of the dry snouts and pure watery tails are not necessarily associated with particle-size segregation, and that a mixture of water and monodisperse grains can also generate them. The research of Gray & Ancey (2009), Johnson *et al.* (2012), Baker *et al.* (2016*a*) and Gray (2018) on the formation of coarse granular fronts in bi-disperse granular flows, does, however, point to a promising approach to account for their formation, by incorporating shear and the layered development of the flow into debris flow models.

In this paper, a depth-averaged fluid–solid mixture model with shear is derived, which assumes the flow has three regimes consisting of (i) dry grains, (ii) a mixture of water and grains, and (iii) pure water. The concentrations of the grains and water within regimes (i)–(iii) are set *a priori* in (4.6)–(4.8). The volume fraction of water ϕ^w can therefore take
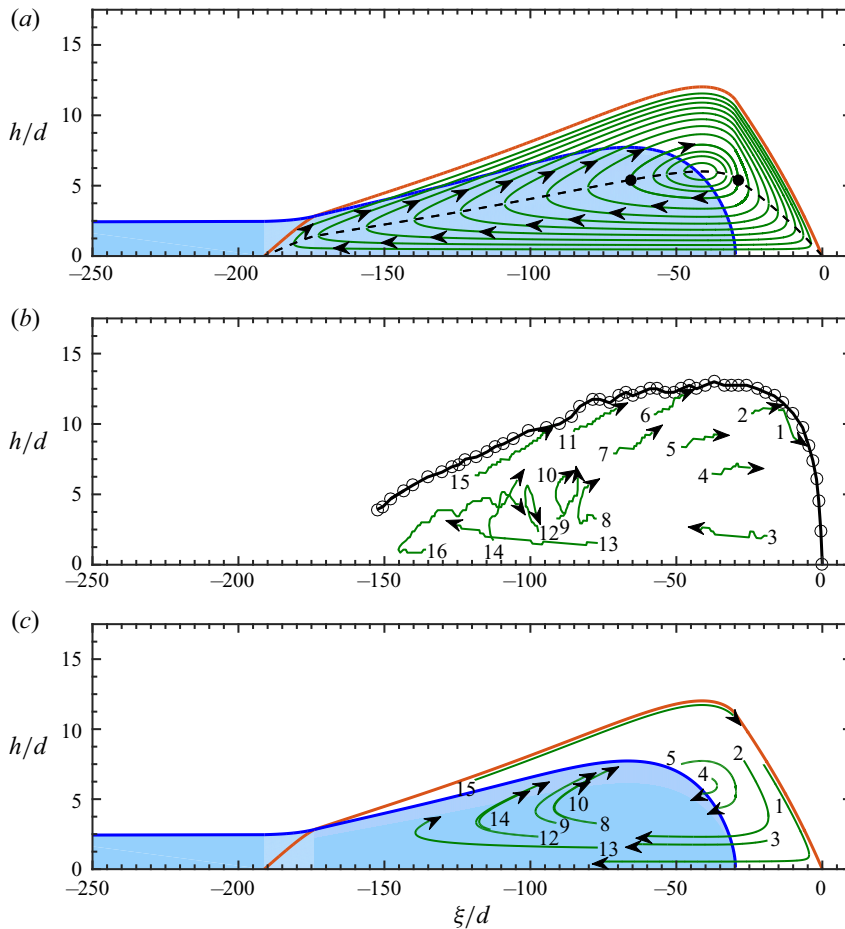
Figure 6. (*a*) Nested (green) streamlines within the granular region for the same conditions as illustrated in figure 5(*b*). The granular free surface is illustrated in brown and the no-mean-flow line in the frame of the wave is shown with a dashed line. The water is shaded in blue. Each streamline has two intersections with the no-mean-flow line (as illustrated by the black markers on one loop). Grains that lie above the no-mean-flow line move forwards towards the front of the flow, while grains below it move backwards towards the tail. (*b*) Measured particle paths in Davies' (1990) experiments over a one-second time interval (green arrowed lines) and the measured free surface height (circles). (*c*) Predicted particle paths using the flow field in panel (*a*). In panel (*c*), the original positions of grains with numbers (1) and (2) are $(-20.1326d, 7.4855d)$ and $(-26.9030d, 7.7656d)$, respectively, which are different from those in panel (*b*) due to the fact that their measured positions are beyond the predicted grain surface.

three values 0, $1 - \phi^c$ or 1, where ϕ^c is the solids volume fraction, which is constant and uniform throughout the granular phase. This latter assumption precludes excess pore fluid pressure effects (see Kowalski & McElwaine 2013; Iverson & George 2014; Bouchut *et al.* 2016; Wang *et al.* 2017; Meng & Wang 2018; Meng *et al.* 2020). While the local water and grain concentrations in regimes (i)–(iii) are set in stone, the water height h^w and the grain height h^g are independent fields that determine the local vertical structure. This vertical structure is taken into account in the depth averaging of the granular and water mass and momentum balances. In particular, the volume fraction weighted depth-averaged water velocity $\bar{u}^w$, defined in (4.9*b*), changes as the relative heights of the grains and water change. As a result, if there is a deep layer of pure water (regime iii) on top of a thin layer of

water and grains (regime ii), then the water momentum balance will be more reflective of the momentum balance for a pure water layer. Conversely, if there is only a thin pure water layer, the momentum balance for the water will be closer to that for the water percolating through the grains.

The governing equations are combined into a single unified system (4.67)–(4.77) that can seamlessly switch between dry, oversaturated, undersaturated and pure water regimes. To illustrate the flexibility and power of this approach, comparisons are made to Davies' (1988, 1990) small-scale moving bed flume experiments, which were performed with a mixture of monodisperse grains and water. The travelling-wave solutions constructed here account for Davies' (1988, 1990) findings that if the grain volume exceeds what a steady-uniform flow can sustain at low bed speeds, then a bulbous head develops that is connected to an upstream region of uniform-depth flow (figure 4). At higher bed speeds, the theory naturally generates steadily travelling waves for a finite granular mass that transition from (i) a dry front (ii) to an undersaturated region, (iii) an oversaturated region and finally (iv) a pure watery tail (see figures 5 and 6). These solutions therefore encompass all four debris flow regimes in a single longitudinal profile. Moreover, the free surface profile and the grain trajectories are in good agreement with the experimental data of Davies (1988, 1990), without the use of any fitting parameters. Velocity shear in the granular body allows a continuous circulation of particles, with those higher in the flow advected towards the flow front, and those lower down in the slower moving part of the flow being overtaken by the moving wave until they near the tail of the flow and start moving forwards again. In these solutions, the dry granular front is driven downslope by the upstream water front, which experiences less friction. Conversely, in the tail, a thin layer of water develops that is in steady-uniform flow and the grains experience less basal friction.

The theory derived in this paper is sufficiently general to apply to both quasi-steady flows (Davies 1988, 1990) as well as fully transient spatially developing ones (Iverson 1997; Johnson *et al.* 2012; Taylor-Noonan 2020). In particular, there is no difference in the physical assumptions that need to go into the theory in these cases. The only difference lies in the initial and boundary conditions that are applied to the final model. A future paper will develop a numerical method to solve the full system of depth-averaged equations (4.67)–(4.77) and test the results against transient experiments with strong longitudinal spreading, which is a characteristic feature of natural debris flows. It should be noted, however, that even fully transient spreading flows can locally enter a quasi-steady flow regime if their fronts propagate steadily downslope. This is the case in the large-scale debris-flow experiments of Johnson *et al.* (2012), as well as in the small-scale analogue experiments of Pouliquen (1999*a*), Viroulet *et al.* (2018), Rocha *et al.* (2019) and Edwards *et al.* (2021). The small-scale experimental results of Davies (1988, 1990) and the solutions constructed here in § 5 are therefore of direct relevance to real debris flows.

Author ORCIDs.

Xiannan Meng https://orcid.org/0000-0002-8045-1332;

C.G. Johnson https://orcid.org/0000-0003-2192-3616;

J.M.N.T. Gray https://orcid.org/0000-0003-3554-0499.

Appendix A. No jump in the effective stress tractions

The field equations (2.11) and (2.12) assume that physical quantities are continuous and differentiable. These conditions are not necessarily met on the water surface $z = s^w(x, t)$ in the undersaturated region or the grain surface $z = s^g(x, t)$ in the oversaturated region. In this case, momentum-jump conditions (Chadwick 1976) must be applied across the singular surfaces. The existence of the non-conservative terms, such as the buoyancy force, present a challenge to the direct formulation of jump conditions. However, the assumption of constant solids volume fraction (4.6) made in this paper reduces the buoyancy force to a conservative form in the undersaturated region and the momentum-jump condition at the water free surface is therefore

$$F^w(x, t) = 0 : \quad [\![\varrho^g \boldsymbol{u}^g (\boldsymbol{u}^w - \boldsymbol{u}^g) \cdot \boldsymbol{n}^w + \boldsymbol{\sigma}^g \boldsymbol{n}^w]\!] = 0. \tag{A1}$$

Substitution of the grain partial stress (2.5) into (A1), and using the mass-jump condition (2.17) to simplify the result, implies

$$F^w(x, t) = 0 : \quad [\![M^g \boldsymbol{u}^g - (\phi^c p^{w\star} \mathbf{I} + \boldsymbol{\sigma}^e) \boldsymbol{n}^w]\!] = 0, \tag{A2}$$

where $M^g = \varrho^{g+}(\boldsymbol{u}^w - \boldsymbol{u}^{g+}) \cdot \boldsymbol{n}^w$ is the grain mass flux across the water surface. The normal component of the water surface traction (3.18) implies that, to leading order, the pore fluid pressure is $p^{w\star} = 0$. Substituting this into (A2) implies that

$$F^w(x, t) = 0 : \quad [\![M^g \boldsymbol{u}^g - \boldsymbol{\sigma}^e \boldsymbol{n}^w]\!] = 0. \tag{A3}$$

It follows that if the granular velocity is continuous across the water free surface, then (A3) implies that there is no jump in the effective stress

$$F^w(x, t) = 0 : \quad [\![\boldsymbol{\sigma}^e \boldsymbol{n}^w]\!] = 0. \tag{A4}$$

Using the scaling (3.1a–f) to non-dimensionalise (A4) implies that the tangential and normal components of the granular momentum jump condition are

$$\left[\!\left[-\varepsilon \hat{\sigma}^e_{xx} \frac{\partial \hat{s}^w}{\partial \hat{x}} + \mu \hat{\sigma}^e_{xz} \right]\!\right] = 0, \quad \hat{z} = \hat{s}^w(\hat{x}, \hat{t}), \tag{A5}$$

$$\left[\!\left[-\varepsilon \mu \hat{\sigma}^e_{xz} \frac{\partial \hat{s}^w}{\partial \hat{x}} + \hat{\sigma}^e_{zz} \right]\!\right] = 0, \quad \hat{z} = \hat{s}^w(\hat{x}, \hat{t}). \tag{A6}$$

Appendix B. The undersaturated grain momentum balance

This appendix provides details of the derivation of the depth-averaged granular momentum balance (4.36) in the undersaturated region. It is convenient to define the left-hand side of the non-dimensional downslope granular momentum balance (3.3) as

$$\mathscr{L}^g = \varepsilon \left(\frac{\partial}{\partial \hat{t}}(\phi^g \hat{u}^g) + \frac{\partial}{\partial \hat{x}}(\phi^g \hat{u}^g \hat{u}^g) + \frac{\partial}{\partial \hat{z}}(\phi^g \hat{u}^g \hat{w}^g) \right). \tag{B1}$$

The integral of (B1) through the grain depth is divided into two parts, one integral above the water free surface $\hat{z} = \hat{s}^w$, and one below it. Using Leibniz's integration rule

to swap the order of integration and differentiation, and substituting the surface and basal kinematic conditions (3.9) and (3.10), implies

$$\int_{\hat{b}}^{\hat{s}^g} \mathscr{L}^g d\hat{z} = \int_{\hat{b}}^{\hat{s}^w} \mathscr{L}^g \, d\hat{z} + \int_{\hat{s}^w}^{\hat{s}^g} \mathscr{L}^g \, d\hat{z}$$

$$= \varepsilon \frac{\partial}{\partial \hat{t}} (\hat{h}^g \overline{\phi^g \hat{u}^g}) + \varepsilon \frac{\partial}{\partial \hat{x}} (\hat{h}^g \overline{\phi^g (\hat{u}^g)^2}) + \left[\!\!\left[\varepsilon \phi^g \hat{u}^g \left(\frac{\partial \hat{s}^w}{\partial \hat{t}} + \hat{u}^g \frac{\partial \hat{s}^w}{\partial \hat{x}} - \hat{w}^g \right) \right]\!\!\right],$$
(B2)

where (3.13) implies that the terms in the jump bracket $[\![\cdot]\!]$ vanish provided there is no jump in the downslope granular velocity. Using the assumption that the solids volume fraction is constant (4.6), the terms on the right-hand side of (3.3) are

$$\mathscr{R}^g = -\varepsilon \gamma \phi^c \frac{\partial \hat{p}^{w\star}}{\partial \hat{x}} - \varepsilon \frac{\partial \hat{\sigma}_{xx}^e}{\partial \hat{x}} - \mu \frac{\partial \hat{\sigma}_{xz}^e}{\partial \hat{z}} + \phi^c \sin \zeta + \gamma \hat{C}^d (\hat{u}^w - \hat{u}^g).$$
(B3)

This can also now be integrated through the flow depth by dividing the integration into two parts, and recalling that the buoyancy and Darcy drag are active only below the water surface. It follows that

$$\int_{\hat{b}}^{\hat{s}^g} \mathscr{R}^g d\hat{z} = \int_{\hat{b}}^{\hat{s}^w} \mathscr{R}^g \, d\hat{z} + \int_{\hat{s}^w}^{\hat{s}^g} \mathscr{R}^g \, d\hat{z}$$

$$= \hat{h}^g \phi^c \sin \zeta - \varepsilon \frac{\partial}{\partial \hat{x}} (\hat{h}^g \hat{\bar{\sigma}}_{xx}^e) - \varepsilon \gamma \phi^c \frac{\partial}{\partial \hat{x}} (\hat{h}^w \hat{\bar{p}}^w) - \left(\varepsilon \hat{\sigma}_{xx}^e \frac{\partial \hat{b}}{\partial \hat{x}} - \mu \hat{\sigma}_{xz}^e \right)$$

$$- \left[\!\!\left[\varepsilon \hat{\sigma}_{xx}^e \frac{\partial \hat{s}^w}{\partial \hat{x}} - \mu \hat{\sigma}_{xz}^e \right]\!\!\right] - \varepsilon \gamma \phi^c \hat{p}_b^{w\star} \frac{\partial \hat{b}}{\partial \hat{x}} - \int_{\hat{b}}^{\hat{s}^w} \gamma \hat{C}^d (\hat{u}^g - \hat{u}^w) \, d\hat{z}, \quad \text{(B4)}$$

where the surface and basal kinematic conditions, (3.9) and (3.10), and the downslope surface traction (3.15) have been used to simplify the result. The terms within the jump bracket $[\![\cdot]\!]$ vanish, because there is no jump in the effective stress (A5). The combination of (B2) and (B4) gives (4.36).

Appendix C. Derivation of the fluid viscous stress

This appendix provides details of the derivation of the non-dimensional depth-averaged viscous stress experienced by the water. By using the constitutive relation for the deviatoric stress in the Newtonian fluid (2.7), and non-dimensionalising using the scalings (3.1a–f), it follows that

$$\hat{\tau}_{xx}^w = \frac{2\phi^w}{Re} \frac{\partial \hat{u}^w}{\partial \hat{x}},$$
(C1)

where the Reynolds number $Re = \varrho^{w\star} H \sqrt{gH} / \eta^w$. For the undersaturated regime, substituting $\phi^w = 1 - \phi^c$ and using Leibniz's rule for exchanging the order of integration and differentiation, implies that

$$\hat{h}^w \hat{\bar{\tau}}_{xx}^w = \frac{2}{Re} \left(\int_{\hat{b}}^{\hat{s}^w} \phi^w \frac{\partial \hat{u}^w}{\partial \hat{x}} d\hat{z} \right) = \frac{2}{Re} (1 - \phi^c) \left(\frac{\partial}{\partial \hat{x}} (\hat{h}^w \hat{\bar{u}}^w) - \left[\hat{u}^w \frac{\partial \hat{z}}{\partial \hat{x}} \right]_{\hat{b}}^{\hat{z}^w} \right).$$
(C2)

Trying to formally include all of the terms on the right-hand side of (C2) is difficult and leads to theories that are too complicated. A pragmatic approach is to assume that the

943 A19-38

downslope velocity is uniform with depth, i.e. that $\hat{u}^w = \hat{\bar{u}}^w$. In this case, (C2) reduces to

$$\hat{h}^w \hat{\bar{\tau}}_{xx}^w \approx \frac{2}{Re} \hat{h}^w (1 - \phi^c) \frac{\partial \hat{\bar{u}}^w}{\partial \hat{x}}. \tag{C3}$$

In the oversaturated regime, the plug-flow assumption implies that

$$\hat{h}^w \hat{\bar{\tau}}_{xx}^w \approx \frac{2}{Re} (\hat{h}^w - \phi^c \hat{h}^g) \frac{\partial \hat{\bar{u}}^w}{\partial \hat{x}}. \tag{C4}$$

Appendix D. The oversaturated water momentum balance

This appendix provides details of the derivation of the depth-averaged water momentum balance (4.63) in the oversaturated region. It is convenient to define the left-hand side of the non-dimensional downslope water momentum balance (3.7) as

$$\mathcal{L}^w = \varepsilon \left(\frac{\partial}{\partial \hat{t}} (\phi^w \hat{u}^w) + \frac{\partial}{\partial \hat{x}} (\phi^w \hat{u}^w \hat{u}^w) + \frac{\partial}{\partial \hat{z}} (\phi^w \hat{u}^w \hat{w}^w) \right). \tag{D1}$$

Since there is a discontinuity in the water concentration at the grain free surface $\hat{z} = \hat{s}^g$, the integration is split into two parts

$$\int_{\hat{b}}^{\hat{s}^w} \mathcal{L}^w \, d\hat{z} = \int_{\hat{b}}^{\hat{s}^g} \mathcal{L}^w \, d\hat{z} + \int_{\hat{s}^g}^{\hat{s}^w} \mathcal{L}^w \, d\hat{z}. \tag{D2}$$

Using Leibniz's rule to exchange the order of integration and differentiation and the surface and basal kinematics conditions (3.11)–(3.12), it follows that

$$\int_{\hat{b}}^{\hat{s}^w} \mathcal{L}^w \, d\hat{z} = \varepsilon \frac{\partial}{\partial \hat{t}} (\hat{h}^w \overline{\phi^w \hat{u}^w}) + \varepsilon \frac{\partial}{\partial \hat{x}} (\hat{h}^w \overline{\phi^w (\hat{u}^w)^2}) + \left[\!\!\left[\varepsilon \phi^w \hat{u}^w \left(\frac{\partial \hat{s}^g}{\partial \hat{t}} + \hat{u}^w \frac{\partial \hat{s}^g}{\partial \hat{x}} - \hat{w}^w \right) \right]\!\!\right], \tag{D3}$$

where the terms within the jump bracket $[\![\cdot]\!]$ vanish due to (3.14) provided the downslope water velocity is continuous across the concentration discontinuity. Finally, using the definition of the depth-averaged velocity (4.9*b*) and the water shape factor (4.45), the integral of the left-hand side becomes

$$\int_{\hat{b}}^{\hat{s}^w} \mathcal{L}^w \, d\hat{z} = \varepsilon \frac{\partial}{\partial \hat{t}} ((\hat{h}^w - \phi^c \hat{h}^g) \hat{\bar{u}}^w) + \varepsilon \frac{\partial}{\partial \hat{x}} (\chi^w (\hat{h}^w - \phi^c \hat{h}^g) (\hat{\bar{u}}^w)^2). \tag{D4}$$

Below the granular free surface, the right-hand side of (3.7) can be written as

$$\mathcal{R}^w = -\varepsilon \frac{\partial \hat{p}^{w\star}}{\partial \hat{x}} + \varepsilon \phi^c \frac{\partial \hat{p}^{w\star}}{\partial \hat{x}} + \varepsilon^2 \frac{\partial \hat{\tau}_{xx}^w}{\partial \hat{x}} + \frac{\partial \hat{\tau}_{xz}^w}{\partial \hat{z}} + \phi^w \sin \zeta - \hat{C}^d (\hat{u}^w - \hat{u}^g), \tag{D5}$$

using $\phi^w = 1 - \phi^c$. Above the grain free surface, the term $\phi^c \partial \hat{p}^{w*}/\partial \hat{x}$ and the Darcy drag are zero. Using Leibniz's rule to exchange the order of integration and differentiation, the traction-free water condition (3.17), the basal water traction (3.21) and the depth-integrated

Darcy drag (4.54), it follows that

$$
\int_{\hat{b}}^{\hat{s}^w} \mathscr{R}^w \, d\hat{z} = (\hat{h}^w - \phi^c \hat{h}^g) \sin \zeta - C^w \hat{\bar{u}}^w |\hat{\bar{u}}^w| - \hat{C}^d (\hat{\psi}^w (\hat{s}^g) - \hat{h}^g \hat{\bar{u}}^g) - \varepsilon \frac{\partial}{\partial \hat{x}} (\hat{h}^w \hat{\bar{p}}^{w\star})
$$

$$
+ \varepsilon^2 \frac{\partial}{\partial \hat{x}} (\hat{h}^w \hat{\bar{\tau}}_{xx}^w) + \varepsilon \left(\hat{p}^{w\star} \frac{\partial \hat{z}}{\partial \hat{x}} \right)_{\hat{b}}^{\hat{s}^w} + \varepsilon \phi^c \frac{\partial}{\partial \hat{x}} \left(\int_{\hat{b}}^{\hat{s}^g} \hat{p}^{w\star} \, d\hat{z} \right)
$$

$$
- \varepsilon \phi^c \left(\hat{p}^{w\star} \frac{\partial \hat{z}}{\partial \hat{x}} \right)_{\hat{b}}^{\hat{s}^g} - \left[\!\left[\varepsilon \hat{p}^{w\star} \frac{\partial \hat{s}^g}{\partial \hat{x}} - \varepsilon^2 \hat{\tau}_{xx}^w \frac{\partial \hat{s}^g}{\partial \hat{x}} + \hat{\tau}_{xz}^w \right]\!\right], \tag{D6}
$$

where the terms in the jump bracket $[\![\cdot]\!]$ vanish provided there is no jump in stress at the granular free surface. Combining (D4) and (D6) gives the oversaturated depth-averaged water momentum balance (4.61).

REFERENCES

ABRAMOWITZ, M. & STEGUN, I. 1970 *Handbook of Mathematical Functions*, 9th edn, p. 3.3.7. Dover.

ANDERSON, K., SUNDARESAN, S. & JACKSON, R. 1995 Instabilities and the formation of bubbles in fluidized beds. *J. Fluid Mech.* **303**, 327–366.

ANDERSON, T.B. & JACKSON, R. 1967 A fluid mechanical description of fluidized beds: equations of motion. *Ind. Engng Chem. Fundam.* **6**, 527–539.

ARMANINI, A., CAPART, H., FRACCAROLLO, L. & LARCHER, M. 2005 Rheological stratification in experimental free surface flows of granular-liquid mixtures. *J. Fluid Mech.* **532**, 269–319.

BAKER, J.L., JOHNSON, C.G & GRAY, J.M.N.T. 2016*a* Segregation-induced finger formation in granular free surface flows. *J. Fluid Mech.* **809**, 168–212.

BAKER, J.L., JOHNSON, C.G & GRAY, J.M.N.T. 2016*b* A two-dimensional depth-averaged $\mu(I)$-rheology for dense granular avalanches. *J. Fluid Mech.* **787**, 367–395.

BALLANTYNE, C.K. 2002 Paraglacial geomorphology. *Quaternary Sci. Rev.* **21**, 1935–2017.

BAUMGARTEN, A.S. & KAMRIN, K. 2019 A general fluid-sediment mixture model and constitutive theory validated in many flow regimes. *J. Fluid Mech.* **861**, 721–764.

BEAR, J. 1972 *Dynamics of Fluids in Porous Media*. Elsevier.

BERZI, D. & JENKINS, J.T. 2008 A theoretical analysis of free surface flows of saturated granular-liquid mixtures. *J. Fluid Mech.* **608**, 393–410.

BERZI, D. & JENKINS, J.T. 2009 Steady inclined flows of granular-fluid mixtures. *J. Fluid Mech.* **641**, 359–387.

BERZI, D., JENKINS, J.T. & LARCHER, M. 2010 Debris flows: recent advances in experiments and modeling. *Adv. Geophys.* **52**, 103–138.

DE BOER, R. & EHLERS, W. 1990 The development of the concept of effective stresses. *Acta Mechanica* **83**, 77–92.

BOUCHUT, F., FERNADEZ-NIETO, E.D., MANGENEY, A. & NARBONA-REINA, G. 2016 A two-phase two-layer model for fluidized granular flows with dilatancy effects. *J. Fluid Mech.* **801**, 166–221.

BOYER, F., GUAZZELLI, É. & POULIQUEN, O. 2011 Unifying suspension and granular rheology. *Phys. Rev. Lett.* **107**, 188301.

CHADWICK, P. 1976 *Continuum Mechanics. Concise Theory and Problems* (republished 1999). Dover.

CHASSAGNE, R., MAURIN, R., CHAUCHAT, J., GRAY, J.M.N.T. & FREY, P. 2020 Discrete and continuum modelling of grain size segregation during bedload transport. *J. Fluid Mech.* **895**, A30.

CHAUDHRY, M.H. 2008 *Open-Channel Flow*. Springer.

CHERTOCK, A., CUI, S., KURGANOV, A. & WU, T. 2015 Well-balanced positivity preserving central-upwind scheme for the shallow water system with friction terms. *Intl J. Numer. Meth. Fluids* **78**, 355–383.

COSTA, J.E. & WILLIAMS, G.P. 1984 Debris-flow dynamics. *Tech. Rep.* 84-606. US Geological Survey.

DAVIES, T.R.H. 1988 Debris flow surges – a laboratory investigation. *Mitteilungen der Versuchsanstalt fur Wasserbau, Hydrologie und Glaziologie, No. 96* (ed. D. Vischer). Eidgenössischen Technischen Hochschule, Zürich.

DAVIES, T.R.H. 1990 Debris flow surges – experimental simulation. *N. Z. J. Hydrol.* **29**, 18–46.

EDWARDS, A.N., VIROULET, S., JOHNSON, C.G. & GRAY, J.M.N.T. 2021 Erosion-deposition dynamics and long distance propagation of granular avalanches. *J. Fluid Mech.* **915**, A9.

EGASHIRA, E., ITOH, T. & TAKEUCHI, H. 2001 Transition mechanism of debris flows over rigid bed to over erodible bed. *Phys. Chem. Earth* B **26**, 169–174.

EINSTEIN, A. 1906 Calculation of the viscosity-coefficient of a liquid in which a large number of small spheres are suspended in irregular distribution. *Ann. Phys. Leipzig* **19**, 286–306.

ENWALD, H., PELRANO, E. & ALMSTEDT, A.-E. 1996 Eulerian two-phase flow theory applied to fluidization. *Intl J. Multiphase Flow* **22**, 21–66.

FÉLIX, G. & THOMAS, N. 2004 Relation between dry granular flow regimes and morphology of deposits: formation of levées in pyroclastic deposits. *Earth Planet. Sci. Lett.* **221**, 197–213.

FORTERRE, Y. 2006 Kapiza waves as a test for three-dimensional granular flow rheology. *J. Fluid Mech.* **563**, 123–132.

FORTERRE, Y. & POULIQUEN, O. 2003 Long-surface-wave instability in dense granular flows. *J. Fluid Mech.* **486**, 21–50.

GDR-MiDi 2004 On dense granular flows. *Eur. Phys. J.* E **14**, 341–365.

GEORGE, D.L. & IVERSON, R.M. 2011 A two-phase debris-flow model that includes coupled evolution of volume fractions, granular dilatancy and pore-fluid pressure. In *Fifth Intl Conf. on Debris-flow Hazards Mitigation, Mechanics, Prediction and Assessment* (ed. R. Genevois, D.L. Hamilton & A. Prestinizi), pp. 415–424. Universit La Sapienza.

GEORGE, D.L. & IVERSON, R.M. 2014 A depth-averaged debris-flow model that includes the effects of evolving dilatancy. II. Numerical predictions and experimental tests. *Proc. R. Soc. Lond.* A **470**, 1–31.

GOHARZADEH, A., KHALILI, A. & JØRGENSEN, B.B 2005 Transition layer thickness at a fluid-porous interface. *Phys. Fluids* **17**, 057102.

GRAY, J.M.N.T. 2018 Particle segregation in dense granular flows. *Annu. Rev. Fluid Mech.* **50**, 407–433.

GRAY, J.M.N.T. & ANCEY, C. 2009 Segregation, recirculation and deposition of coarse particles near two-dimensional avalanche fronts. *J. Fluid Mech.* **629**, 387–423.

GRAY, J.M.N.T. & EDWARDS, A.N. 2014 A depth-averaged $\mu(I)$-rheology for shallow granular free surface flows. *J. Fluid Mech.* **755**, 503–534.

GRAY, J.M.N.T. & HUTTER, K. 1997 Pattern formation in granular avalanches. *Contin. Mech. Thermodyn.* **9**, 341–345.

GRAY, J.M.N.T. & KOKELAAR, B.P. 2010 Large particle segregation, transport and accumulation in granular free surface flows. *J. Fluid Mech.* **652**, 105–137.

GRAY, J.M.N.T., TAI, Y.C. & NOELLE, S. 2003 Shock waves, dead-zones and particle-free regions in rapid granular free surface flows. *J. Fluid Mech.* **491**, 161–181.

GRAY, J.M.N.T. & THORNTON, A.R. 2005 A theory for particle size segregation in shallow granular free surface flows. *Proc. R. Soc. Lond.* A **461**, 1447–1473.

GRAY, J.M.N.T., WIELAND, M. & HUTTER, K. 1999 Free surface flow of cohesionless granular avalanches over complex basal topography. *Proc. R. Soc. Lond.* A **455**, 1841–1874.

DE HAAS, T., BRAAT, L., LEUVEN, J.R.F.W., LOKHORST, I.R. & KLEINHANS, M.G. 2015 Effects of debris flow composition on runout, depositional mechanisms, and deposit morphology in laboratory experiments. *J. Geophys. Res.* **120**, 1949–1972.

HIGMAN, B., *et al.* 2018 The 2015 landslide and tsunami in Taan Fiord, Alaska. *Sci. Rep.* **8**, 12993.

HOGG, A.J. & PRITCHARD, D. 2004 The effects of hydraulic resistance on dam-break and other shallow inertial flows. *J. Fluid Mech.* **501**, 179–212.

HUNGR, O. 2000 Analysis of debris flow surges using the theory of uniformly progressive flow. *Earth Surf. Process. Landf.* **25**, 483–495.

IVERSON, R.M. 1997 The physics of debris flows. *Rev. Geophys.* **35**, 245–296.

IVERSON, R.M. 2003 The debris-flow rheology myth. In *Debris-Flow Hazards Mitigation: Mechanics, Prediction, and Assessment* (ed. D. Richenmann & C.L. Chen), pp. 303–314. Millpress.

IVERSON, R.M. & DENLINGER, R.P. 2001 Flow of variably fluidized granular masses across three-dimensional terrain. 1. Coulomb mixture theory. *J. Geophys. Res.* **106**, 537–552.

IVERSON, R.M. & GEORGE, D.L. 2014 A depth-averaged debris-flow model that includes the effects of evolving dilatancy. I. Physical basis. *Proc. R. Soc. Lond.* A **470**, 20130819.

IVERSON, R.M., LOGAN, M., LAHUSEN, R.G. & BERTI, M. 2010 The perfect debris flow? Aggregated results from 28 large-scale experiments. *J. Geophys. Res.* **115**, F03005.

JACKSON, R. 2000 *The Dynamics of Fluidized Particles*. Cambridge University Press.

JOHNSON, C.G., KOKELAAR, B.P., IVERSON, R.M., LOGAN, M., LaHUSEN, R.G. & GRAY, J.M.N.T. 2012 Grain-size segregation and levee formation in geophysical mass flows. *J. Geophys. Res.* **117**, F01032.

JOP, P., FORTERRE, Y. & POULIQUEN, O. 2006 A constitutive relation for dense granular flows. *Nature* **44**, 727–730.

JOSEPH, D. & LUNGDREN, T. 1990 Ensemble averaged and mixture theory equations for incompressible fluid-particle suspensions. *Intl J. Multiphase Flow* **16**, 35–42.

KEAN, J.W., MCCOY, S.W., TUCKER, G.E., STALEY, D.M. & COE, J.A. 2013 Runoff-generated debris flows: observations and modeling of surge initiation, magnitude, and frequency. *J. Geophys. Res.* **118**, 2190–2207.

KEAN, J.W., STALEY, D.M., LANCASTER, J.T., RENGERS, F.K., SWANSON, B.J., COE, J.A., HERNANDEZ, J.L., SIGMAN, A.J., ALLSTADT, K.E. & LINDSAY, D.N. 2019 Inundation, flow dynamics, and damage in the 9 January 2018 montecito debris-flow event, California, USA: opportunities and challenges for post-wildfire risk assessment. *Geosphere* **15**, 1140–1163.

KOKELAAR, B.P., GRAHAM, R.L., GRAY, J.M.N.T. & VALLANCE, J.W. 2014 Fine-grained linings of leveed channels facilitate runout of granular flows. *Earth Planet. Sci. Lett.* **385**, 172–180.

KOWALSKI, J. & MCELWAINE, J.N. 2013 Shallow two-component gravtity-driven flows with verticla variation. *J. Fluid Mech.* **714**, 434–462.

KURGANOV, A. & TADMOR, E. 2000 New high-resolution central schemes for nonlinear conservation laws and convection-diffusion equations. *J. Comput. Phys.* **160**, 214–282.

LANZONI, S., GREGORETTI, C. & STANCANELLI, L.M. 2017 Coarse-grained debris flow dynamics on erodible beds. *J. Geophys. Res.* **122**, 592–614.

LEONARDI, A., CABRERA, M., WITTEL, F.K., KAITNA, R., MENDOZA, M., WU, W. & HERRMANN, H.J. 2015 Granular-front formation in free surface flow of concentrated suspensions. *Phys. Rev.* E **92**, 052204.

LIU, W., HE, S.M., CHEN, Z., YAN, S.X. & DENG, Y. 2021 Effect of viscosity changes on the motion of debris flow by considering entrainment. *J. Hydraul. Res.* **59**, 120–135.

MANGENEY, A., BOUCHUT, F., THOMAS, N., VILOTTE, J.P. & BRISTEAU, M.O. 2007 Numerical modeling of self-channeling granular flows and of their levee-channel deposits. *J. Geophys. Res.* **112**, F02017.

MANNING, R. 1891 On the flow of water in open channel and pipes. *Trans. Inst. Civ. Engrs Ireland* **20**, 161–207.

MAURIN, R., CHAUCHAT, J. & FREY, P. 2016 Dense granular flow rheology in turbulent bedload transport. *J. Fluid Mech.* **804**, 490–512.

MCSAVENEY, M.J., BEETHAM, R.D. & LEONARD, G.S. 2005 The 18 May 2005 debris flow disaster at matata: causes and mitigation suggestions. *Tech. Rep.* 2005/71. Institute of Geology and Nuclear Sciences.

MENG, X. & WANG, Y. 2016 Modelling and numerical simulation of two-phase debris flows. *Acta Geotech.* **11**, 1027–1045.

MENG, X. & WANG, Y. 2018 Modeling dynamic flows of grain–fluid mixtures by coupling the mixture theory with a dilatancy law. *Acta Mechanica* **229**, 2521–2583.

MENG, X., WANG, Y., CHIOU, M.C. & ZHOU, Y. 2020 Investigation of influence of an obstacle on granular flows by virtue of a depth-integrated theory. *Eur. J. Mech.* B/*Fluids* **84**, 334–349.

MORLAND, L.W. 1992 Flow of viscous fluids through a porous deformable matrix. *Surv. Geophys.* **13**, 209–268.

MURISIC, N., PAUSADER, B., PESCHKA, D. & BERTOZZI, A. 2013 Dynamics of particle settling and resuspension in viscous liquid films. *J. Fluid Mech.* **717**, 203–231.

NUNZIATO, J., PASSMAN, S., GIVLER, C., MACTIGUE, D. & BRADY, J. 1986 Continuum theories for suspensions. In *Advancements in Aerodynamics, Fluid Mechanics and Hydraulics (Proc. ASCE Special. Conf., Minneapolis, Minn.)* (ed. R. Arndt, A. Stefan, C. Farrell & S.N. Peterson), pp. 465–472. ASCE Publications.

OURIEMI, M., AUSSILLOUS, P. & GUAZZELLI, É. 2009 Sediment dynamics. Part 1. Bed-load transport by laminar shearing flows. *J. Fluid Mech.* **636**, 295–319.

PAILHA, M. & POULIQUEN, O. 2008 A two-phase flow description of the initiation of underwater granular avalanches. *J. Fluid Mech.* **633**, 115–135.

PELANTI, M., BOUCHUT, F. & MANGENEY, A. 2008 A roe-type scheme for two-phase shallow granular flows over variable topography. *ESAIM: Math. Model. Numer. Anal.* **42**, 851–885.

PIERSON, T.C. 1986 Flow behavior of channelized debris flows, mount St. Helens. In *Hillslope Processes* (ed. A.D. Abrahams), pp. 269–296. Allen and Unwin.

PITMAN, E.B. & LE, L. 2005 A two-fluid model for avalanche and debris flows. *Phil. Trans. R. Soc.* A **363**, 1573–1601.

POULIQUEN, O. 1999*a* On the shape of granular flows down rough inclined planes. *Phys. Fluids* **11**, 1956–1958.

POULIQUEN, O. 1999*b* Scaling laws in granular flows down rough inclined planes. *Phys. Fluids* **11**, 542–548.

POULIQUEN, O. & FORTERRE, Y. 2002 Friction law for dense granular flows: application to the motion of a mass down a rough inclined plane. *J. Fluid Mech.* **453**, 133–151.

PUDASAINI, S. 2012 A general two–phase debris flow model. *J. Geophys. Res.* **117**, F03010.

REN, D. 2014 The devastating Zhouqu storm-triggered debris flow of August 2010: likely causes and possible trends in a future warming climate. *J. Geophys. Res.* **119**, 3643–3662.

ROCHA, F.M., JOHNSON, C.G. & GRAY, J.M.N.T. 2019 Self-channelisation and levee formation in monodisperse granular flows. *J. Fluid Mech.* **876**, 591–641.

SATI, V.P. 2022 Glacier bursts-triggered debris flow and flash flood in Rishi and Dhauli Ganga valleys: a study on its causes and consequences. *Nat. Hazards Res.* **2**, 33–40.

SAVAGE, S.B. & HUTTER, K. 1989 The motion of a finite mass of granular material down a rough incline. *J. Fluid Mech.* **199**, 177–215.

SCHEIDL, C., MCARDELL, B.W. & RICKENMANN, D. 2015 Debris-flow velocities and superelevation in a curved laboratory channel. *Can. Geotech. J.* **52**, 305–317.

TAYLOR-NOONAN, A.M. 2020 Mechanisms of particle-liquid interaction in high-mobility debris flows. PhD thesis, Queen's University.

TERZAGHI, K. 1943 *Theoretical Soil Mechanics*. John Wiley & Sons.

TRUESDELL, C. 1984 *Rational Thermodynamics*. Springer.

TRULSSON, M., ANDREOTTI, B. & CLAUDIN, P. 2012 Transition from the viscous to inertial regime in dense suspensions. *Phys. Rev. Lett.* **109**, 118305.

TURNBULL, B., BOWMAN, E.T. & MCELWAINE, J.N. 2015 Debris flows: experiments and modelling. *C. R. Phys.* **16**, 86–96.

VALLANCE, J.W. & SAVAGE, S.B. 2000 Particle segregation in granular flows down chutes. In *IUTAM Symposium on Segregation in Granular Materials* (ed. A.D. Rosato & D.L. Blackmore). Kluwer.

VIROULET, S., BAKER, J.L., ROCHA, F.M., JOHNSON, C.G., KOKELAAR, B.P. & GRAY, J.M.N.T. 2018 The kinematics of bidisperse granular roll waves. *J. Fluid Mech.* **848**, 836–875.

WANG, C., WANG, Y., PENG, C. & MENG, X. 2017 Dilatancy and compaction effects on the submerged granular column collapse. *Phys. Fluids* **29**, 103307.

WANG, F., WU, Y-H., YANG, H., TANIDA, Y. & KAMEI, A. 2015 Preliminary investigation of the 20 August 2014 debris flows triggered by a severe rainstorm in Hiroshima city, Japan. *Geoenvironmental Disasters* **2**, 17.

WOODHOUSE, M.J., THORNTON, A.R., JOHNSON, C.G., KOKELAAR, B.P. & GRAY, J.M.N.T. 2012 Segregation-induced fingering instabilities in granular free surface flows. *J. Fluid Mech.* **709**, 543–580.